

Semi-Blind Post-Equalizer SINR Estimation and Dual CSI Feedback for Radar-Cellular Coexistence

Raghunandan M. Rao, *Student Member, IEEE*, Vuk Marojevic, *Senior Member, IEEE*, Jeffrey H. Reed, *Fellow, IEEE*

Abstract

Current cellular systems use pilot-aided statistical-channel state information (S-CSI) estimation and limited feedback schemes to aid in link adaptation and scheduling decisions. However, in the presence of pulsed radar signals, pilot-aided S-CSI is inaccurate since interference statistics on pilot and non-pilot resources can be different. Moreover, the channel will be *bimodal* as a result of the periodic interference. In this paper, we propose a max-min heuristic to estimate the post-equalizer SINR in the case of non-pilot pulsed radar interference, and characterize its distribution as a function of noise variance and interference power. We observe that the proposed heuristic incurs low computational complexity, and is robust beyond a certain SINR threshold for different modulation schemes, especially for QPSK. This enables us to develop a comprehensive *semi-blind* framework to estimate the wideband SINR metric that is commonly used for S-CSI quantization in 3GPP Long-Term Evolution (LTE) and New Radio (NR) networks. Finally, we propose *dual CSI feedback* for practical radar-cellular spectrum sharing, to enable accurate CSI acquisition in the *bimodal channel*. We demonstrate significant improvements in throughput, block error rate and retransmission-induced latency for LTE-Advanced Pro when compared to conventional pilot-aided S-CSI estimation and limited feedback schemes.

Index Terms

Post-equalizer SINR, Semi-blind Techniques, Max-min Heuristic, Dual CSI Feedback, Radar-Cellular Coexistence.

Raghunandan M. Rao and Jeffrey H. Reed are with Wireless@VT, the Bradley Department of ECE, Virginia Tech, Blacksburg, VA, 24061, USA (email: {raghumr, reedjh}@vt.edu).

Vuk Marojevic is with the Department of ECE, Mississippi State University, Mississippi State, MS, 39762, USA (e-mail: vuk.marojevic@ece.msstate.edu).

The support of the U.S. National Science Foundation (NSF) Grants CNS-1564148 and CNS-1642873 are gratefully acknowledged.

I. INTRODUCTION

In order to mitigate severe spectrum shortage in sub-6 GHz bands and meet the exponentially increasing demand for user data, spectrum sharing has been proposed. In sub 6-GHz frequency bands, radar systems are the major primary consumers of spectrum, where most commercial cellular and wireless LAN (WLAN) systems currently operate. Spectrum sharing with radars is efficient because of its waveform characteristics, and sparse deployment. In particular, spectrum sharing with *pulsed radar systems* is more desirable because of the interference-free time duration that can be leveraged for secondary user operations.

In the United States, the Federal Communications Commission (FCC) has ratified the rules for radar-communications coexistence in the 3550-3650 MHz [1] and 5 GHz [2] bands. More recently, the radar-incumbent 1.3 GHz [3] and 3450-3550 MHz [4] bands have also been identified for spectrum sharing. Due to these ongoing developments, cellular standardization has evolved into support for operation in unlicensed frequency bands, such as License Assisted Access (LAA) [5] and the Third Generation Partnership Project (3GPP) 5G New Radio-Unlicensed (5G NR-U) standards.

In addition, vehicular communications are supported by cellular radio access technologies (RAT). More recently, 3GPP Release 14 introduced the cellular vehicle-to-everything (C-V2X) protocol [6], which can operate either in the 5.9 GHz band, or the cellular operator's licensed band [7]. Therefore, C-V2X systems would also have to share spectrum with other wireless systems such as Wi-Fi and radar. In particular, high-powered radars operating in the 5 GHz Unlicensed National Information Infrastructure B (U-NII B) bands [2] can cause adjacent channel interference to C-V2X systems.

Often, cooperation between radar and cellular systems is (a) impractical in the case of outdated civilian radar systems, and (b) impossible with military radars due to security concerns. In addition, due to the rapid progress of cellular technology compared to that of radar systems, the burden of harmonious coexistence is usually placed on cellular systems, which is the premise for this paper.

A. Related Work

Prior works have proposed harmonious radar-cellular coexistence mechanisms in different operational regimes using multi-antenna techniques, waveform optimization, and opportunistic spectrum access. Multi-antenna techniques exploit the spatial degrees of freedom to minimize

mutual interference, and methods such as subspace projection [8], [9], robust beamforming [10], and MIMO matrix completion [11] have been investigated in the past. These works assume the availability of accurate channel state information at the radar and/or the cellular system, which is often infeasible, especially in the case of spectrum sharing with military radars.

Radar waveform optimization approaches using mutual information (MI)-based metrics have been investigated in [12] to mitigate interference to secondary users. In addition, new multicarrier waveforms such as Precoded SUBcarrier Nulled-Orthogonal Frequency Division Multiplexing (PSUN-OFDM) [13], and FREquency SHift (FRESH)-filtered OFDM [14] have been proposed to improve their resilience to pulsed interference. Unfortunately, these waveforms require significant changes to existing radar systems and cellular standards, which makes their implementation infeasible in the near future.

Opportunistic spectrum sharing approaches have also been studied in the context of spectrum sharing with a *rotating radar* [15], [16], that leverages partial or complete information about the radar behavior to maximize spectral utilization in time/frequency/spatial dimensions. However these are not easily applicable to systems such as search-and-track radars.

Numerical and experimental studies of underlay radar-LTE spectrum sharing scenarios [17], [18] have demonstrated that practical LTE deployments can operate with negligible degradation with an exclusion zone radius of tens of kilometers, which is significantly smaller than what is used in current deployments. However in these regimes, the pulsed radar intermittently impairs the cellular signal, disrupting data resources and critical control mechanisms of the cellular system.

B. Motivation

Statistical-CSI (S-CSI) such as channel spatial covariance and *post-equalizer SINR* [20] are important quantities, forming the basis of link adaptation and user scheduling schemes in modern wireless communication systems. LTE and NR systems use *pilot-aided* S-CSI estimation schemes, and limited feedback mechanisms to balance link-level performance with feedback overhead [19], [21]. Since pilots occupy a tiny fraction (at most 5%) of time-frequency resources in cellular signals, pilot-aided S-CSI is accurate if interference and fading statistics are the same on pilot and non-pilot resources. While this is generally true in conventional cellular deployments, it does not hold in the presence of pulsed interference.

TABLE I
SIMULATION PARAMETERS: UNDERLAY SPECTRUM SHARING BETWEEN AN LFM PULSED RADAR AND LTE-A PRO
DOWNLINK

Parameter	Description
3GPP Releases	8 to 14 (LTE to LTE-A Pro)
Center Frequency	2 GHz
System Bandwidth	10 MHz
Transmission Mode	TM 0 (SISO) from Port 0 [19]
Small-scale Fading	Extended Pedestrian A (EPA) Doppler frequency $f_d = 10$ Hz
CSI feedback mode	Periodic and Wideband
CSI estimation interval [19]	10 ms
CSI delay	8 ms
HARQ mode	Asynchronous and Non-Adaptive with up to 4 retransmissions
Radar Pulse repetition Interval	3.125 ms
Radar pulse width (T_{pul})	$5 \mu\text{s}$
Radar relative carrier frequency offset (Δf_r)	0 Hz
Radar sweep frequency (f_s)	5 MHz

We illustrate this using the example of a linear frequency modulated (LFM) pulsed radar coexisting with the LTE-A Pro downlink between a single evolved NodeB (eNB) and a single user equipment (UE). The system parameters shown in Table I. The baseband transmitted waveform of the LFM radar is given by [22]

$$i_{\text{LFM}}(t) = \sqrt{P_{\text{rad}}} e^{j\left(\frac{\pi f_s t}{T_{\text{pul}}} + 2\pi \Delta f_r\right)t} \text{ for } -\frac{T_{\text{pul}}}{2} \leq t \leq \frac{T_{\text{pul}}}{2}, \quad (1)$$

where P_{rad} is the radar transmitted power, T_{pul} is the radar pulse width, f_s the sweep frequency, and Δf_r the offset w.r.t. the center frequency of the cellular signal.

Fig. 1a illustrates the fundamental issue: Since pulsed radar interference is time-selective, absence of pilot interference results in inaccurate pilot-aided SINR estimates. As shown in Fig. 1b and 1c, this leads to degradation of throughput and block error rate performance in the case of commonly used limited feedback schemes: minimum, median and maximum CSI feedback (explained in Section II). Note that at the eNB, the criteria for choosing the modulation and

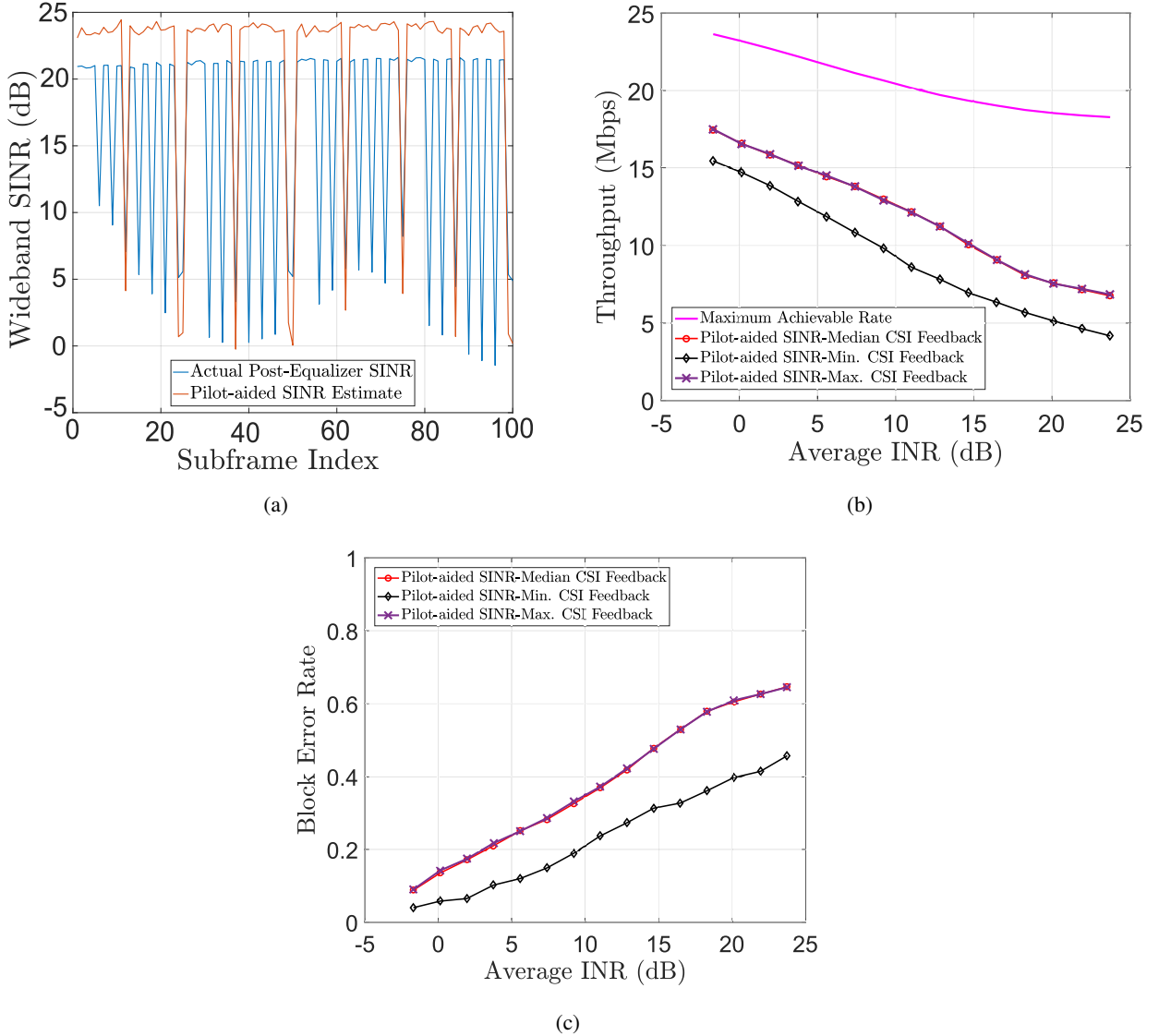


Fig. 1. Illustration of (a) inaccurate pilot-aided SINR estimates due to pulsed radar interference, and degradation of (b) throughput, and (c) block error rate (BLER) performance. The average SNR of the eNB-to-UE fading channel is 19.5 dB.

coding scheme (MCS) is to maximize rate while satisfying $\text{BLER} \leq 0.1$ [6]. The maximum achievable rate (pink curve) in Fig. 1b is the maximum rate achieved (using the maximum MCS) under the constraint that average $\text{BLER} = 0.1$.

Similar observations have been demonstrated in [23], where *non-pilot interference* was shown to significantly affect SINR estimates, resulting in the degradation of link adaptation performance. In addition, results from [24] have shown lower link-level performance because of inaccurate CSI estimates in pulsed radar-LTE coexistence. Our prior work [25] rigorously proved that the

S-CSI acquired for the *interference channel* is inaccurate for a wide range of radar repetition intervals.

In such scenarios, blind SINR estimation methods need to be used since they do not rely on pilot signals. Prior works have investigated maximum likelihood (ML) [26], [27], moment-based [28], and cyclostationary-based [29] SINR estimation methods. However, the accuracy of ML and moment-based methods depend on the availability of accurate fading and interference statistics of the channel, which is often infeasible to acquire in real-time. For cyclostationarity-aided methods, short length of the cyclic prefix, unequal power allocation across subcarriers, and dependence of its accuracy on long-term averaging (for thousands of OFDM symbols) hinder their application to practical scenarios. Moreover, these methods do not estimate the *post-equalizer* SINR¹, which is the metric used to aid scheduling decisions and link adaptation procedures in LTE and NR [20].

In addition to inaccurate SINR estimates in Fig. 1a, we observe that the channel is *bimodal*, due to periodic transitions between ‘*interference-free*’ and ‘*interference-impaired*’ states. Since limited feedback procedures in LTE and NR support single CSI feedback for a given frequency subband, it is fundamentally impossible to quantize the bimodal nature of the channel using a single value.

C. Contributions

In this paper, we make the following contributions:

- 1) We present a robust max-min heuristic to estimate the post-equalizer SINR with low complexity, and characterize its distribution under a realistic tractable signal model for quadrature amplitude modulated (QAM) symbols. We analyze its accuracy and robustness, to demonstrate its applicability for radar-impaired OFDM symbols in practical spectrum sharing scenarios (section III).
- 2) We propose a comprehensive framework to estimate the radar parameters, and combine pilot-aided as well as heuristic-aided SINR estimates to calculate the wideband post-equalizer SINR metric (section IV).

¹Post-equalizer SINR refers to the SINR of the received signal after channel estimation and equalization stages of the baseband receiver [20], [30].

- 3) We propose ‘*dual CSI feedback*’ as a simple extension to currently used limited CSI feedback mechanisms in cellular systems, to support CSI acquisition for ‘*fading*’ and ‘*interference-impaired*’ channel states (section V).
- 4) Using radar-LTE-A Pro spectrum sharing as an example, we demonstrate significant improvements in rate, BLER and retransmission-induced latency using our proposed framework, when compared to conventional *pilot-aided SINR* and *single CSI feedback* schemes (section V).

The rest of this paper is organized as follows. Section II provides the system model, and describes the basics of CSI estimation and limited feedback schemes used in LTE and NR. Section III describes the max-min heuristic, derives its distribution under a tractable signal model, and analyzes its accuracy and robustness. Section IV introduces the semi-blind SINR estimation framework, and evaluates its performance. Section V develops the dual CSI feedback mechanism, discusses the incurred overhead, and demonstrates its effectiveness through link-level simulation results for radar-LTE-A Pro coexistence scenarios. Finally, section VI concludes the paper, and discusses directions for future research.

II. SYSTEM MODEL AND PRELIMINARIES

A. Cellular Downlink Signal Model

We consider an underlay radar-cellular spectrum sharing scenario, where the cellular downlink coexists with a *wideband pulsed radar system*. For ease of exposition, we consider a single base station (with N antenna ports) serving a single user (with K antenna ports). The cellular downlink is OFDM-based with N_{sub} subcarriers, where data is transmitted in blocks composed of T OFDM symbols. The received signal vector on the k^{th} subcarrier of the n^{th} OFDM symbol (referred to as a resource element (RE)) indexed by an ordered pair (n, k) , $\mathbf{z}_k[n] \in \mathbb{C}^K$, is given by

$$\mathbf{z}_k[n] = \mathbf{H}_k[n]\mathbf{W}_k[n]\mathbf{x}_k[n] + \mathbf{h}_{r,k}[n]i_k[n] + \mathbf{w}_k[n], \quad (2)$$

where $\mathbf{H}_k[n] \in \mathbb{C}^{K \times N}$ is the downlink channel matrix, $\mathbf{W}_k[n] \in \mathbb{C}^{N \times L}$ the precoding matrix, and L the data vector length. The transmitted symbol vector is chosen from $\mathbf{x}_k[n] \in \mathcal{X}^L$, where \mathcal{X} is the set of symbols for the given modulation scheme. The noise vector is i.i.d. such that $\mathbf{w}_k[n] \sim \mathcal{CN}(0, \sigma_w^2 \mathbf{I}_K)$. After transmit beamforming, the radar-to-user channel vector on the $(n, k)^{\text{th}}$ resource elements (RE) is $\mathbf{h}_{r,k}[n] \in \mathbb{C}^K$, and the baseband-equivalent interference symbol is $i_k[n]$ such that $\mathbb{E}[\mathbf{h}_{r,k}[n]i_k[n]] = \mathbf{0}$ and $\mathbb{E}[\mathbf{h}_{r,k}[n]i_k[n]i_k^*[n]\mathbf{h}_{r,k}^H[n]] = \mathbf{R}_{\mathbf{I},k}[n]$. For ease

of notation we suppress the RE index henceforth, while noting that the symbol on each RE is processed in a similar manner.

If $\hat{\mathbf{H}}$ is the estimated channel matrix and $\hat{\sigma}_w^2$ the estimated noise variance, then the decoded data symbol $\hat{\mathbf{x}}$ using a minimum mean square error (MMSE) equalizer² is given by

$$\hat{\mathbf{x}} = (\mathbf{W}^H \hat{\mathbf{H}}^H \hat{\mathbf{H}} \mathbf{W} + \hat{\sigma}_w^2 \mathbf{I}_K)^{-1} \mathbf{W}^H \hat{\mathbf{H}}^H \mathbf{y}. \quad (3)$$

Defining $\hat{\mathbf{G}}_{\text{MMSE}} \triangleq (\mathbf{W}^H \hat{\mathbf{H}}^H \hat{\mathbf{H}} \mathbf{W} + \hat{\sigma}_w^2 \mathbf{I}_L)^{-1} \mathbf{W}^H \hat{\mathbf{H}}^H$, the instantaneous SINR $\hat{\gamma}_l$ for the transmitted symbol on the l^{th} antenna port ($1 \leq l \leq L$) is

$$\hat{\gamma}_l = \frac{|x_l|^2}{\left| [(\hat{\mathbf{G}}_{\text{MMSE}} \mathbf{H} \mathbf{W} - \mathbf{I}_L) \mathbf{x} + \hat{\mathbf{G}}_{\text{MMSE}} (\mathbf{h}_r i + \mathbf{w})]_l \right|^2}, \quad (4)$$

where $[\mathbf{z}]_l$ denotes the l^{th} element of \mathbf{z} . Since $\hat{\gamma}_l$ is calculated after baseband processing, it is termed as the *post-equalizer/post-processing SINR*. This is used to calculate link quality metrics [20], which subsequently aid in scheduling decisions and link adaptation schemes.

B. Pilot-Aided SINR Estimation and Wideband SINR Metrics

Typically, pilot signals are used both for channel estimation as well as for SINR estimation³. In this work, we use the pilot-aided linear MMSE estimation method described in [31] assuming unit powered pilot symbols. For interference-free pilots in a MIMO transmission mode, the pilot-aided MMSE post-equalizer SINR estimate on the l^{th} antenna port ($\hat{\gamma}_{p,l}$) is given by [32]

$$\hat{\gamma}_{p,l} = \frac{1}{\left[\frac{\mathbf{W}^H \hat{\mathbf{H}}^H \hat{\mathbf{H}} \mathbf{W}}{\hat{\sigma}_w^2} + \mathbf{I}_L \right]_{l,l}^{-1}} - 1, \quad (5)$$

where $[\mathbf{X}]_{i,i}$ denotes the i^{th} element on the main diagonal of matrix \mathbf{X} , and p in the subscript of $\hat{\gamma}_{p,l}$ denotes that it is a pilot-aided SINR estimate. Since a data block comprises of contiguous time and frequency resource elements, a *subband/wideband SINR metric* is often calculated to quantize the CSI. If the SINR estimate on the $(n, k)^{\text{th}}$ RE is $\hat{\gamma}[n, k]$, the wideband SINR is

²In practical systems, other linear equalizers such as Zero-Forcing (ZF) or Regularized ZF are also commonly used to recover the data symbols.

³3GPP Releases up to LTE-A Pro can use the common reference signal (CRS) and the demodulation reference signal (DMRS) to estimate the channel as well as the SINR. However, pilot signals such as the CSI reference signal (CSI-RS) can only be used to estimate the optimal precoder and SINR.

obtained using standard mapping functions such as effective exponential SINR mapping ($\hat{\gamma}_e$) [33] and average SINR mapping ($\hat{\gamma}_a$) [34], given by

$$\hat{\gamma}_e = \log \left[\sum_{(n,k) \in \mathcal{D}} \frac{e^{-\frac{\hat{\gamma}[n,k]}{\beta}}}{|\mathcal{D}|} \right]^{-\beta} \quad \text{and} \quad \hat{\gamma}_a = \sum_{(n,k) \in \mathcal{D}} \frac{\hat{\gamma}[n,k]}{|\mathcal{D}|} \quad (6)$$

respectively, where \mathcal{D} denotes the RE indices of data symbols in the cellular signal, and β is a function of the modulation scheme [33].

C. Link Adaptation Using Limited CSI Feedback

LTE and NR adapt the multi-antenna transmission mode (SISO/diversity/SU-MIMO/MU-MIMO), modulation format, and error control coding scheme, as a function of the channel fading and interference conditions. In order to limit the overhead while balancing performance, they support limited CSI feedback that is generally estimated over a finite estimation window, called the *CSI estimation window*⁴. The quantized CSI value consists of the following quantities:

- 1) Precoding Matrix Indicator (PMI): an index of $\mathbf{W}_k \in \mathcal{W}$ chosen from a codebook \mathcal{W} of predefined matrices.
- 2) Rank Indicator (RI): the maximum rank supported on the downlink channel, which can be inferred from \mathbf{W}_k .
- 3) Channel Quality Indicator (CQI): a 4-bit value representing the quantized subband/wideband post-equalizer SINR metric (6) of the cellular signal.

The CQI is mapped to a 5-bit modulation and coding scheme (MCS). In the LTE and NR PHY layer, decoding success and PHY layer metrics are characterized on units of data known as *transport blocks*. For each transport block, the MCS denotes the most spectrally efficient scheme that simultaneously ensures that a maximum block error rate (BLER) is not exceeded on average. In addition, L is equal to the number of transport blocks allotted to a single user, and $L \leq 2$ in LTE and NR even when the number of antenna ports $K \geq 2$ [19], [21]. For ease of exposition, we refer to the wideband SINR metric of a data block as the *post-equalizer SINR* henceforth.

If $\hat{\gamma}[m]$ is the post-equalizer SINR calculated for the m^{th} data block, then $CQI[m] = f(\hat{\gamma}[m]) \in \mathbb{N}$ is the corresponding CQI, where $f(\cdot)$ is a monotonically non-decreasing function of SINR.

⁴The estimation window duration is chosen based on the rate at which the channel statistics vary, depending on user mobility. In typical cellular deployments, this interval ranges from tens to hundreds of milliseconds [21].

Considering a CSI estimation window of length T_{CSI} data blocks, the wideband CQI measurements corresponding to the T_{CSI} subframes are collectively represented by the vector $\mathbf{CQI} = [CQI[0], CQI[1], \dots, CQI[T_{CSI} - 1]] \in \mathbb{N}^{T_{CSI}}$. In this work, we consider the following conventional CSI quantization and limited feedback schemes:

- 1) minimum CSI feedback, where $\min(\mathbf{CQI})$ is periodically fed back after every T_{CSI} data blocks, and
- 2) median CSI feedback, where $\text{med}(\mathbf{CQI})$ is periodically fed back after every T_{CSI} data blocks.
- 3) maximum CSI feedback, where $\max(\mathbf{CQI})$ is periodically fed back after every T_{CSI} data blocks.

It is evident from Fig. 1 that $\min(\cdot)$, $\text{med}(\cdot)$ and $\max(\cdot)$ quantization functions result in overoptimistic CQI values due to inaccurate pilot-aided SINR estimates. In addition, it is important to note that pilot-aided SINR estimates are accurate (a) in the absence of interference, and (b) when a pilot-bearing OFDM symbol is interference-impaired. Therefore, a key challenge is to accurately estimate the post-equalizer SINR with low computational complexity when pilot-resources are interference-free but data resources are not. In this work, we consider potential interference of pilots that are used to estimate the channel response as well as the SINR⁵. In the subsection below, we discuss the post-equalizer signal model of an interference-impaired non-pilot OFDM symbol, when the downlink channel is accurately estimated by interference-free pilot signals.

D. Baseband Equivalent Post-Processed Signal Model

Using equation (3), the resultant post-equalizer baseband signal on subcarrier k will be

$$\hat{\mathbf{x}}_k = \hat{\mathbf{G}}_{\text{MMSE},k} \mathbf{H}_k \mathbf{W}_k \mathbf{x}_k + \hat{\mathbf{G}}_{\text{MMSE},k} \mathbf{h}_{r,k} i_k + \hat{\mathbf{G}}_{\text{MMSE},k} \mathbf{w}_k. \quad (7)$$

To develop a tractable analytical model, we make the following assumptions.

Assumption 1. *In a coherence block of K_{RB} subcarriers, the post-equalized signal on each antenna in the presence of accurate channel estimates can be written as*

$$y_k = x_k + \sqrt{P_{r,k}} e^{j\phi_k} + n_k, \quad (8)$$

⁵In cellular standards up to LTE-A Pro, the same pilot signal is used for channel estimation as well as SINR estimation, such as the cell-specific reference signal (CRS). Other pilots such as Demodulation Reference Signals (DMRS) can also be used to estimate the SINR, *conditioned on the precoding matrix* (\mathbf{W}) used [21].

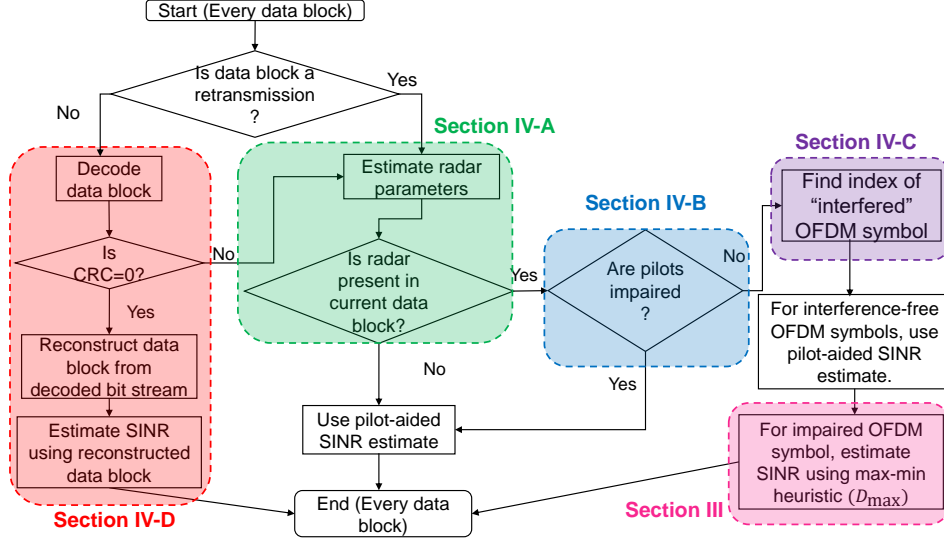


Fig. 2. Flowchart of the hybrid SINR estimation framework for the cellular downlink in the presence of a pulsed radar. The SINR estimation algorithm is executed for every data block.

where $P_{r,k}$ and ϕ_k is the post-equalizer interference power and phase, and $n_k \sim \mathcal{CN}(0, \sigma_n^2)$ is the additive white gaussian noise. The transmitted symbol $x_k \sim \mathcal{U}[\mathcal{X}]$, where \mathcal{X} is the set of QAM symbols, and $\mathcal{U}[\cdot]$ denotes the uniform distribution.

Assumption 2. Interference power $P_{r,k}$ is constant in the coherence block $k \in \{k_0 + 1, k_0 + 2, \dots, k_0 + K_{RB}\}$.

Assumption 3. In the coherence block $k \in \{k_0 + 1, k_0 + 2, \dots, k_0 + K_{RB}\}$ the interference phase is i.i.d. distributed as $\phi_k \sim \mathcal{U}(0, 2\pi)$.

Assumption 1 approximates equation (7) in a coherence block by an *interference-impaired AWGN channel* on antenna port l using $[\hat{\mathbf{x}}_k]_l = y_k, [(\hat{\mathbf{G}}_{\text{MMSE},k} \mathbf{H}_k \mathbf{W}_k - \mathbf{I}_L) \mathbf{x}_k + \hat{\mathbf{G}}_{\text{MMSE},k} \mathbf{h}_{r,k} i_k]_l = \sqrt{P_{r,k}} e^{j\phi_k}$, and $[\hat{\mathbf{G}}_{\text{MMSE},k} \mathbf{w}_k]_l = n_k$.

Assumption 2 is accurate in a coherence block for LFM radar signals⁶ with $f_s T_{\text{pul}} \gg 1$ where the radar spectrum is approximated by [22]

$$I_{\text{LFM}}(f) \approx \sqrt{\frac{P_{\text{rad}} T_{\text{pul}}}{f_s}} e^{-j\left(\frac{\pi T_{\text{pul}} (f - \Delta f_r)^2}{f_s} + \frac{\pi}{4}\right)} \quad (9)$$

⁶This approximation is accurate in a coherence block of width ~ 100 kHz, in the case of a continuous-wave (CW) radar.

For an arbitrarily chosen contiguous subcarrier sequence $\{f_i\}$ for $i = 1, 2, \dots, K_{RB}$ and $\Delta f_r = 0$, assumption 3 approximates the sequence of square-law phase terms using

$$\left\{ \frac{\pi T_{\text{pul}}(k+i)^2 \Delta f^2}{f_s} \right\} \stackrel{\text{i.i.d.}}{\sim} \mathcal{U}[0, 2\pi], i = 1, \dots, K_{RB}, \quad (10)$$

after marginalization over a broad range of $0 \leq k \leq (N_{\text{sub}} - (K_{RB} + 1))f_s$, and T_{pul} , where Δf is the subcarrier spacing. Note that this approximation is used for ease of exposition, and the general form of the distribution is derived in the next section for scenarios when the phase offset of the radar interference is known.

E. Post-Equalizer SINR Estimation Framework

To accurately estimate the wideband SINR metric in equation (6), the receiver must be able to detect the presence of interference and localize its position in the time-frequency grid, so that the appropriate SINR estimate can be used for each RE. In this work, we propose a comprehensive framework to accurately estimate the post-equalizer SINR of a data block. Fig. 2 shows the flowchart of the proposed framework, which is composed of the following key stages:

- 1) Estimation of the radar repetition rate, which is used by the receiver to predict when radar interference will occur in the future.
- 2) Detection of pulsed radar interference on pilot-bearing OFDM symbols, which is used by the receiver to determine the accuracy of pilot-aided SINR estimate for the interference channel.
- 3) Detection of the contaminated OFDM symbol index. The receiver uses the *max-min heuristic-aided SINR estimation method* only for the interference-impaired data-bearing OFDM symbol.

In the following section, we characterize the properties of the proposed max-min heuristic that blindly estimates the post-equalizer SINR of a coherence block blindly in the presence of accurate downlink channel estimates, and the rest of the framework will be discussed in section IV.

III. LOW COMPLEXITY MAX-MIN HEURISTIC TO ESTIMATE POST-EQUALIZER SINR

To estimate the *post-equalizer interference and noise amplitude* in a coherence block of contiguous subcarrier indices $\{1, 2, \dots, K_{RB}\}$, the heuristic D_{max} is defined as the maximum of the distance between a received symbol and its nearest neighboring constellation point, given by

$$D_{\text{max}} = \max_{k=1,2,\dots,K_{RB}} \min_{x^{(j)} \in \mathcal{X}} \|y_k - x^{(j)}\|_2. \quad (11)$$

It is important to note that the additional complexity incurred is due to the \max operation, since calculating the nearest neighbor distance is already a part of the downlink baseband processing chain in modern cellular systems. Therefore, the maximum *minimum distance* calculated over a small coherence block of K_{RB} REs incurs an additional computational complexity of $O(N_{RB}K_{RB})$, where N_{RB} is the number of coherence blocks in the OFDM symbol. The cumulative distribution function (CDF) of D_{\max} can be written as $F_{D_{\max}}(d) = \Pr[D_{\max} \leq d]$, $d \geq 0$. Defining the nearest-neighbor distance of the received symbol on the l^{th} subcarrier as $D_l \triangleq \min_{x^{(j)} \in \mathcal{X}} \|y_l - x^{(j)}\|_2$, after defining $y \triangleq y_R + jy_I$, $n \triangleq n_R + jn_I$, and $x^{(j)} \triangleq x_R^{(j)} + jx_I^{(j)} \in \mathcal{X}$, the nearest neighbor distance can be simplified as

$$D = [(x_R - x_R^{(j)} + \sqrt{P_r} \cos \phi + n_R)^2 + (x_I - x_I^{(j)} + \sqrt{P_r} \sin \phi + n_I)^2]^{1/2}. \quad (12)$$

The following proposition denotes the marginal distribution of D_l ($F_{D_l}(d)$) as a function of interference power P_r , and noise variance σ_n^2 .

Proposition 1. *The CDF of D can be written as*

$$F_{D_l}(d) = \sum_{x \in \mathcal{X}} \int_{\mathcal{A}_\Phi} \int_{\mathcal{A}_{n_R}} \int_{\mathcal{A}_{n_I}} \mathbb{1}[D_l \leq d|x, n, \phi] p_X(x) f_\Phi(\phi) f_{N_R}(n_R) f_{N_I}(n_I) d\phi dn_R dn_I, d \geq 0, \quad (13)$$

where $\mathbb{1}[\cdot]$ denotes the indicator function, $x \sim \mathcal{U}[\mathcal{X}]$, $p_X(x)$ is the probability mass function of $x \in \mathcal{X}$, $f_\Phi(\phi)$ is the density function of the radar phase ϕ , $f_{N_R}(n_R)$ and $f_{N_I}(n_I)$ are the density functions of the real and imaginary components of noise, respectively. The corresponding integration regions are \mathcal{A}_Φ , \mathcal{A}_{n_R} and \mathcal{A}_{n_I} , respectively.

Proof. The event $\{D_l \leq d|x, n, \phi\}$ is represented by the indicator function $\mathbb{1}[\cdot]$. Using the fact that the interference power P_r , phase ϕ and the real and imaginary components of noise are independent of each other, we obtain the desired result when the event of interest is integrated over the appropriate regions of ϕ , n_R and n_I . ■

The marginal distribution of D_{\max} is given in the following theorem.

Theorem 1. *If the interference phase relationship is known, and given by $\phi_i = h_i(\phi_1)$, where $\phi_1 \sim \mathcal{U}[0, 2\pi]$ is the phase of the first symbol in the coherence block and $i = 2, 3, \dots, K_{RB}$, the marginal CDF of D_{\max} is*

$$F_{D_{\max}}(d) = \frac{1}{2\pi|\mathcal{X}|^{K_{RB}}} \int_0^{2\pi} \prod_{l=1}^{K_{RB}} \left[\sum_{x_l \in \mathcal{X}} F_{D_l}(d|x_l, \phi_1) \right] d\phi_1.$$

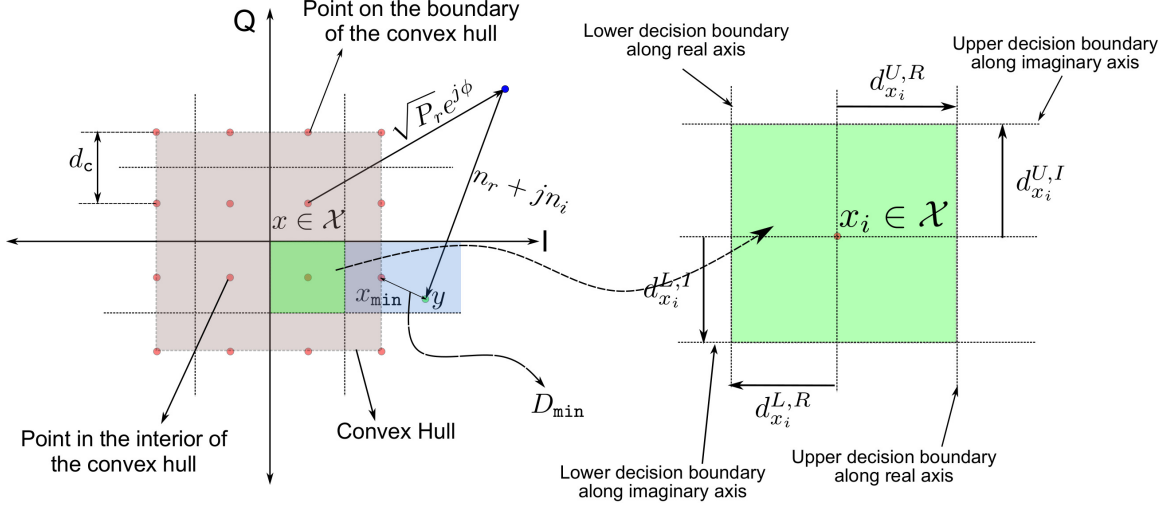


Fig. 3. Illustration of transformation of the input to output symbols via interference and noise addition, and the resulting minimum distance $D_{\min} = \|y - x_{\min}\|_2$. The decision region of x_{\min} is shaded in light blue. The lower figure shows the decision boundaries for $x_i \in \mathcal{X}$ in the constellation diagram.

Proof. The marginal CDF of D_{\max} can be written as

$$F_{D_{\max}}(d) = \int_0^{2\pi} \sum_{\mathbf{x} \in \mathcal{X}^{K_{RB}}} \mathbb{P}[\max(\mathbf{D}) \leq d | \mathbf{x}, \phi] p_{\mathbf{X}}(\mathbf{x}) f_{\Phi}(\phi) d\phi, \quad (14)$$

where $\mathbf{D} = [D_1, \dots, D_{K_{RB}}]$ and $\mathbf{x} = [x_1, \dots, x_{K_{RB}}] \sim \mathcal{U}[\mathcal{X}^{K_{RB}}]$. We have $\{\max(\mathbf{D}) \leq d\} \Leftrightarrow \bigcap_{l=1}^{K_{RB}} \{D_l \leq d\}$. Since the phase relationship is deterministic when conditioned on ϕ_1 , the minimum distances (D_l) are conditionally independent. Marginalizing over the densities of \mathbf{X} and Φ , and simplifying equation (14), we obtain the desired result. ■

In the case of the i.i.d. interference phase model, all the underlying random variables are independent of each other. Dropping the subcarrier index for notational simplicity, the marginal distribution is obtained using results from order statistics of i.i.d. random variables:

$$F_{D_{\max}}(d) = [F_D(d)]^{K_{RB}}, d \geq 0. \quad (15)$$

Based on their location w.r.t. the convex hull of the constellation, the transmitted symbols are classified as (a) interior points (denoted by set \mathcal{X}_{int}) and (b) boundary points (denoted by set \mathcal{X}_{bnd}), where $\mathcal{X}_{\text{bnd}} \cap \mathcal{X}_{\text{int}} = \emptyset$.

Fig. 3 illustrates the transformation of the baseband transmitted signal due to interference and noise. For a QAM scheme with average unit power per symbol, let the minimum distance

TABLE II
DECISION REGION BOUNDARIES FOR CONSTELLATION POINTS IN THE FIRST QUADRANT OF 16-QAM

$x_i \in \mathcal{X}_{16\text{QAM}}$	$d_{x_i}^{L,R}$	$d_{x_i}^{U,R}$	$d_{x_i}^{L,I}$	$d_{x_i}^{U,I}$
$\frac{1}{\sqrt{10}}(1+j)$	$-\frac{1}{\sqrt{10}}$	$\frac{1}{\sqrt{10}}$	$-\frac{1}{\sqrt{10}}$	$\frac{1}{\sqrt{10}}$
$\frac{1}{\sqrt{10}}(1+3j)$	$-\frac{1}{\sqrt{10}}$	$\frac{1}{\sqrt{10}}$	$-\frac{1}{\sqrt{10}}$	∞
$\frac{1}{\sqrt{10}}(3+j)$	$-\frac{1}{\sqrt{10}}$	∞	$-\frac{1}{\sqrt{10}}$	$\frac{1}{\sqrt{10}}$
$\frac{1}{\sqrt{10}}(3+3j)$	$-\frac{1}{\sqrt{10}}$	∞	$-\frac{1}{\sqrt{10}}$	∞

between two points be d_c . If the nearest neighbor of y is $x^{(j)} \in \mathcal{X}_{\text{int}}$, then $0 \leq D \leq \frac{d_c}{\sqrt{2}}$. On the other hand, if $x^{(j)} \in \mathcal{X}_{\text{bnd}}$, then $0 \leq D \leq \infty$. For each $x \in \mathcal{X}$, we define its decision region \mathcal{A}_x given by

$$\mathcal{A}_x = \{(z_x, z_y) | \Re(x) + d_x^{L,R} \leq z_x \leq \Re(x) + d_x^{U,R}, \Im(x) + d_x^{L,I} \leq z_y \leq \Im(x) + d_x^{U,I}\}, \quad (16)$$

where $\Re(x)$ denotes the real part and $\Im(x)$ the imaginary part of complex scalar x . The decision region parameters $d^{L,R}, d^{L,I}, d^{U,R}, d^{U,I}$ for constellation points in the first quadrant of 16-QAM are shown in Table II and illustrated in the bottom portion of Fig. 3. In the following lemma, we derive the conditional distribution of $\{D|X, \Phi\}$.

Lemma 1. *The conditional distribution of $\{D|X, \Phi\}$ is given by*

$$F_D(d|x, \phi) = \begin{cases} \sum_{x^{(j)} \in \mathcal{X}} \left[1 - Q_1\left(\frac{\sqrt{2}\nu_j}{\sigma_n}, \frac{\sqrt{2}d}{\sigma_n}\right) \right] & \text{if } 0 \leq d \leq \frac{d_c}{2} \\ \sum_{x^{(j)} \in \mathcal{X}} \int_0^d \int_{\mathcal{A}_\theta(x^{(j)}, z)} \frac{z}{\pi\sigma_n^2} e^{-\frac{z^2 + \nu_j^2 + 2m_j z}{\sigma_n^2}} d\theta dz & \text{if } \frac{d_c}{2} < d \leq \frac{d_c}{\sqrt{2}} \\ F_D\left(\frac{d_c}{\sqrt{2}}|x, \phi\right) + \sum_{x^{(j)} \in \mathcal{X}_{\text{bnd}}} \int_0^d \int_{\mathcal{A}_\theta(x^{(j)}, z)} \frac{z}{\pi\sigma_n^2} e^{-\frac{z^2 + \nu_j^2 + 2m_j z}{\sigma_n^2}} d\theta dz & \text{otherwise.} \end{cases} \quad (17)$$

where $m_j = m_{R,j} \cos \theta + m_{I,j} \sin \theta$, $\nu_j = (m_{R,j}^2 + m_{I,j}^2)^{1/2}$, $m_{R,j} = x_R - x_R^{(j)} + \sqrt{P_r} \cos \phi$, $m_{I,j} = x_I - x_I^{(j)} + \sqrt{P_r} \sin \phi$, and $Q_M(a, b)$ is the Marcum Q-function with parameters M, a and b [35]. The region of integration for Θ is given by $\mathcal{A}_\theta(x^{(j)}, z) = \{\theta | d_{x^{(j)}}^{L,R} \leq z \cos \theta \leq d_{x^{(j)}}^{U,R}, d_{x^{(j)}}^{L,I} \leq z \sin \theta \leq d_{x^{(j)}}^{U,I}, 0 \leq z \leq d\}$.

Proof. Refer Appendix A. ■

By marginalizing $\{D|X, \Phi\}$ over $\{X, \Phi\}$, the distribution of D is given by

$$F_D(d) = \begin{cases} \frac{1}{2\pi|\mathcal{X}|} \sum_{x \in \mathcal{X}} \sum_{x^{(j)} \in \mathcal{X}} \int_0^{2\pi} \left[1 - Q_1\left(\frac{\sqrt{2}\nu_j}{\sigma_n}, \frac{\sqrt{2}d}{\sigma_n}\right)\right] d\phi, & \text{if } 0 \leq d \leq \frac{d_c}{2}, \\ F_D\left(\frac{d_c}{2}\right) + \sum_{x \in \mathcal{X}} \sum_{x^{(j)} \in \mathcal{X}} \int_0^{\frac{d_c}{2}} \int_{\frac{d_c}{2}}^d \int_{\mathcal{A}_\theta(x_j, z)} \frac{z}{2\pi^2|\mathcal{X}|\sigma_n^2} e^{-\frac{z^2 + \nu^2 + 2m_j z}{\sigma_n^2}} dz d\theta d\phi & \text{if } \frac{d_c}{2} \leq d \leq \frac{d_c}{\sqrt{2}} \\ F_D\left(\frac{d_c}{\sqrt{2}}\right) + \sum_{x \in \mathcal{X}} \sum_{x^{(j)} \in \mathcal{X}_{\text{bnd}}} \int_0^{\frac{d_c}{\sqrt{2}}} \int_{\frac{d_c}{\sqrt{2}}}^d \int_{\mathcal{A}_\theta(x_j, z)} \frac{z}{2\pi^2|\mathcal{X}|\sigma_n^2} e^{-\frac{z^2 + \nu^2 + 2m_j z}{\sigma_n^2}} dz d\theta d\phi & \text{otherwise.} \end{cases} \quad (18)$$

Using it in (15), we obtain the distribution of D_{\max} under the i.i.d. interferer phase model. To characterize the robustness and accuracy of the interference-plus-noise power estimate, we define the following metrics.

Definition 1. *Overestimation probability, defined as $P_{\text{overest}}(P_r, \sigma_n^2) = \mathbb{P}[D_{\max} \geq \sqrt{P_r + \sigma_n^2}]$, is the probability that D_{\max} overestimates the interference-plus-noise compared to the average interference-plus-noise power.*

Definition 2. *Accuracy, defined as $\mathbb{P}\left[\left|\log_{10}\left(\frac{D_{\max}^2}{P_r + \sigma_n^2}\right)\right| \leq \delta\right]$, is the probability that the estimate of interference-plus-noise-power lies within a range of $\pm\delta$ (dB) of the actual value.*

A higher overestimation probability implies a more robust SINR estimate. As we will see in section V-B, SINR estimation using the proposed heuristic results in robust link adaptation in the presence of pulsed radar interference.

A. Numerical Results

Fig. 4a shows the theoretical and simulated distributions of D_{\max} for different values of P_r and σ_n^2 , and 16-QAM modulated data symbols with a coherence block length of $K_{RB} = 12$ are used. We observe that there is very good agreement between the theoretical and numerical results, validating the accuracy of equations (13)-(18). In order to study the estimation accuracy, mismatch in interference-plus-noise of the heuristic compared to that of the average interference-plus-noise power is plotted in Fig. 4b for 16-QAM symbols. We observe that the SINR mismatch in the interference-impaired OFDM symbol is within ± 5 dB for more than 90% of the range of typical SINR values (-5 to 30 dB) encountered in cellular communications. However, in typical scenarios where at most a single radar pulse impacts a data block, mismatch in the wideband SINR metric ($\gamma_{\text{avg}}/\gamma_{\text{esm}}$) due to the robust heuristic will be partially mitigated by the availability

of accurate pilot-aided SINR estimates for *interference-free OFDM symbols*, as discussed in the following section.

Fig. 4c shows the probability of overestimation as a function of (P_r, σ_n^2) for different QAM schemes. We observe that the robustness of the heuristic decreases when the modulation order increases from QPSK to 64-QAM, and that $P_{\text{overest}}(P_r, \sigma_n^2) \geq 0.9$ for QPSK. The reason for this trend can be intuitively explained by considering the following.

If the transmitted symbol is $x \in \mathcal{X}_{\text{bnd}}$, the received symbol y will have a high probability of lying outside the convex hull. In this case, if the nearest neighbor lies on the convex hull and is $x' \in \mathcal{X}_{\text{bnd}}$, $\|y - x\|_2$ and $\|y - x'\|_2$ will have the same order of magnitude. In other words, the penalty due to nearest-neighbor association (i.e. x' instead of x) will be minimal.

On the other hand, for any $x \in \mathcal{X}$, if the nearest neighbor lies within the convex hull i.e. $x' \in \mathcal{X}_{\text{int}}$, then a constellation with a higher minimum distance (d_c) will be more robust. Since $\|y - x'\| \leq d_c/2$, constellations with a higher d_c intrinsically has a higher probability of overestimating $\|y - x\|_2$.

Since QPSK (a) has the highest minimum distance of $d_{c,\text{QPSK}} = 1/\sqrt{2}$, and (b) has all points lying on the convex hull, the max-min heuristic is more robust when compared to that for 16-QAM and 64-QAM.

B. Accuracy and Robustness as a Function of K_{RB}

Intuitively, decreasing K_{RB} reduces the overestimation probability of the heuristic. This behavior can be mathematically explained as follows. Since $F_D(d) \in [0, 1]$, increasing K_{RB} decreases the value of the CDF $\mathbb{P}[D_{\text{max}} \leq d]$, thereby increasing $\mathbb{P}[D_{\text{max}} \geq d]$. Since robustness is characterized by the overestimation probability $\mathbb{P}[D_{\text{max}} \geq \sqrt{P_r + \sigma_n^2}]$, by setting $d = \sqrt{P_r + \sigma_n^2}$, we see that decreasing K_{RB} decreases $\mathbb{P}[D_{\text{max}} \geq \sqrt{P_r + \sigma_n^2}]$ and vice-versa. Fig. 4d shows the robustness (probability of overestimating interference-plus-noise-power) of the heuristic for 16-QAM as a function of K_{RB} , for different values of (P_r, σ_n^2) .

In contrast, it is not straightforward to infer the dependence of accuracy on K_{RB} using mathematical arguments and hence, we use numerical studies to do the same. Figures 4e-4h show the accuracy as a function of δ (dB) for $K_{RB} \in \{4, 8, 12, 16\}$, for different values of (P_r, σ_n^2) . We observe that (a) accuracy is not a monotonic function of K_{RB} , and (b) the optimal K_{RB} that maximizes the accuracy of the SINR estimate depends on (P_r, σ_n^2) , as well as the accuracy threshold δ . In addition, we notice that (a) in high SINR regimes, a low K_{RB} ensures

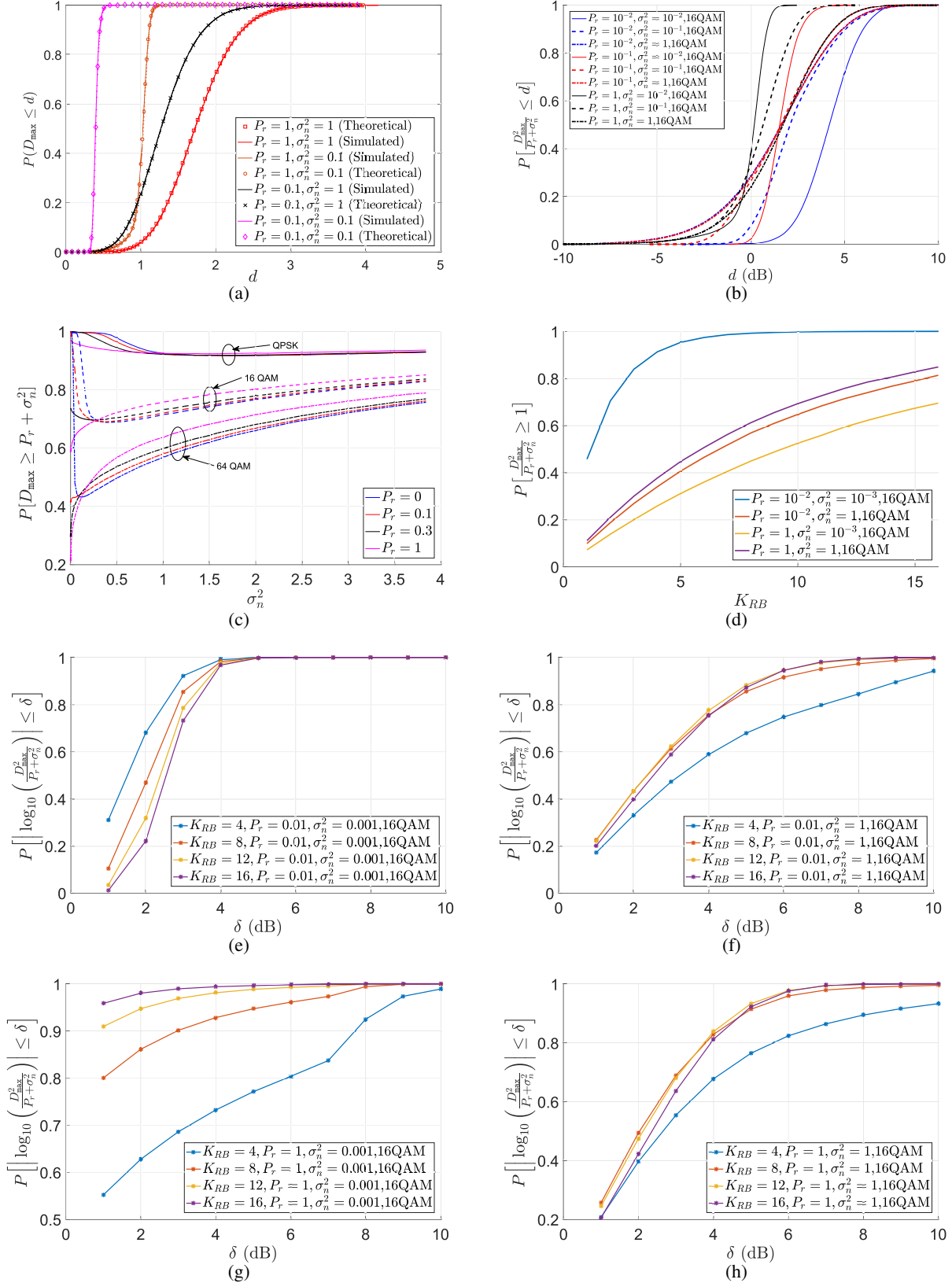


Fig. 4. (a) Comparison of the simulated and theoretical distribution of D_{\max} (equations (13)-(18)) for 16-QAM, (b) distribution of $D_{\max}^2 / (P_r + \sigma_n^2)$ for 16-QAM, and (c) probability of overestimation $P_{\text{overrest}}(P_r, \sigma_n^2)$ for QPSK, 16-QAM and 64-QAM, (d) $P_{\text{overrest}}(P_r, \sigma_n^2)$ as a function of K_{RB} , and the accuracy metric for $K_{RB} \in \{4, 8, 12, 16\}$ for (e) $(P_r, \sigma_n^2) = (10^{-2}, 10^{-3})$, (f) $(P_r, \sigma_n^2) = (10^{-2}, 1)$, (g) $(P_r, \sigma_n^2) = (1, 10^{-3})$, and (h) $(P_r, \sigma_n^2) = (1, 1)$.

high accuracy (Fig. 4e), (b) in interference-limited scenarios (high P_r and low σ_n^2), a high K_{RB} value ensures high accuracy (Fig. 4g), and (c) in intermediate noise and interference conditions, a K_{RB} value of 8 – 16 yields similar accuracy performance (Figs. 4f and 4h).

Similar trends are observed for QPSK and 64-QAM. Unfortunately, a comprehensive mathematical analysis of the accuracy is beyond the scope of this paper. The key takeaway from Figures 4e-4h is that there is no universal K_{RB} value that maximizes the accuracy of the heuristic-aided SINR estimate. However, memory-based schemes that leverage knowledge of interference and noise conditions in the recent past, can be used to choose K_{RB} to balance the robustness and accuracy of the heuristic-aided SINR estimate.

Remark 1. *It is worthwhile to observe that the max-min heuristic is independent on the multi-carrier waveform used, and yields accurate SINR estimates of a coherence block in the received signal.*

IV. SEMI-BLIND/HYBRID POST-EQUALIZER SINR ESTIMATION FRAMEWORK

In this section, we describe the ‘*semi-blind/hybrid*’ post-equalizer SINR estimation framework, which uses pilot-aided (Section II-B) as well as heuristic-aided (Section III) SINR estimates.

Let the data block contain N_{blk} OFDM symbols⁷, \mathcal{A}_{NP} be the set of non-pilot OFDM symbol indices, and $k \in \mathcal{K}[m]$ be the subcarrier indices of data resource elements in the m^{th} OFDM symbol. The SINR of the RE on the k^{th} subcarrier of the n^{th} OFDM symbol can be estimated using

$$\hat{\gamma}[n, k] = \begin{cases} \hat{\gamma}_p[n, k] & \text{for } n = 1, 2, \dots, N_{\text{blk}}, \mathbb{1}[n], \text{ and } n \notin \mathcal{A}_{NP} \\ \hat{\gamma}_p[n, k] & \text{if } n \neq m, \mathbb{1}[m], \text{ and } m \in \mathcal{A}_{NP} \\ \frac{1}{D_{\max}[m, k]} & \text{if } \mathbb{1}[n] \text{ and } n \in \mathcal{A}_{NP}, \end{cases} \quad (19)$$

where $\mathbb{1}[m]$ denotes the occurrence of pulsed radar interference on the m^{th} OFDM symbol, $D_{\max}[m, k]$ is the heuristic for every RE in the coherence block of the contaminated OFDM symbol. If the coherence block contains K_{RB} subcarriers, then $D_{\max}[m, lK_{RB} + 1] = \dots = D_{\max}[m, (l + 1)K_{RB}]$ for $l \in \mathbb{Z}$.

⁷In LTE and NR, the data block is termed as the transport block, which is often sent over a subframe consisting of 14 OFDM symbols.

To determine the appropriate SINR estimate to be used, the contaminated OFDM symbol needs to be known. As shown in Fig. 2, the following intermediate stages are necessary to acquire this information in practice:

- 1) Pulsed radar parameter estimation,
- 2) Detection of the pilot symbol interference, and
- 3) Detection of contaminated OFDM symbol index.

A. Pulsed Radar Parameter Estimation

Most pulsed radars have a fixed repetition interval (T_{rep}) for an extended duration of time (timescale of seconds). Since the interference is periodic, T_{rep} can be estimated by applying Fourier techniques on time-series data of received power per data block, resulting in a low-complexity baseband implementation. Subsequently, the UE can predict future subframes indices which will be impaired by radar interference.

B. Threshold-based Detection of Pilot Interference

Interference on pilot symbols result in accurate SINR estimates [23]. Pilot interference can be detected by monitoring pilot-aided SINR estimates in every data block. For the k^{th} data block, the receiver calculates the wideband SINR metric $\hat{\gamma}_{\text{avg},p}[k]$ using pilot-aided methods. Using knowledge of T_{rep} and pilot-aided SINR estimates of previous data blocks, the wideband SINR metric for non-pilot radar interference ($\hat{\gamma}_{\text{NPI},p}$) is computed. If the current (k^{th}) block is impaired by interference, then

- 1) if $\hat{\gamma}_{\text{NPI},p} - \hat{\gamma}_{\text{avg},p}[k] \geq \gamma_{\text{th}}$, the k^{th} block is considered to be impaired by pilot interference, and
- 2) if $\hat{\gamma}_{\text{NPI},p} - \hat{\gamma}_{\text{avg},p}[k] < \gamma_{\text{th}}$, the k^{th} block is considered to be impaired by non-pilot interference.

In practice, a typical value of the threshold is $\gamma_{\text{th}} = 1$ dB, since the channel quality indicator (CQI) remains the same with a high probability for a SINR mismatch of ± 1 dB [20].

C. Log Likelihood-based Detection of the Interference-Impaired OFDM Symbol

OFDM has a long symbol duration ($72 \mu\text{s}$ in sub-6 GHz bands of LTE and NR). Hence, for wideband radars with a short pulse width ($T_{\text{pul}} \sim 1 \mu\text{s}$), the probability of two adjacent

Algorithm 1 Detection of Corrupted OFDM Symbol Index

1: **Input:** In each data block,

Set of non-pilot OFDM symbol indices \mathcal{A}_{NP}

Data subcarriers of n^{th} OFDM symbol $\mathcal{K}[n]$

Post-processed OFDM symbols $y[n, k] \forall n \in \mathcal{A}_{NP}, k \in \mathcal{K}[n]$

2: Find nearest neighbor of each $y[n, k]$ using $\hat{x}_{\text{nn}}[n, k] = \arg \min_{x \in \mathcal{X}} \|y[n, k] - x\|_2 \forall n \in \mathcal{A}_{NP}, k \in \mathcal{K}[n]$.

3: For each (n, k) , obtain the pilot-aided SINR $\hat{\gamma}_p[n, k]$ using (5).

4: The contaminated OFDM symbol index (\hat{n}) is detected by minimizing the log-likelihood function using

$$\hat{n} = \arg \min_{n \in \mathcal{A}_{NP}} \frac{-1}{|\mathcal{K}[n]|} \sum_{k \in \mathcal{K}[n]} \hat{\gamma}_p[n, k] |y[n, k] - \hat{x}_{\text{nn}}[n, k]|^2. \quad (20)$$

5: Go back to step 1 in the next data block.

OFDM symbols being contaminated is *almost zero*⁸ for sub-6 GHz cellular systems. Therefore, we ignore the possibility of multiple adjacent OFDM symbols being interfered.

We use a log likelihood-based approach to detect the contaminated data-bearing OFDM symbol in every block, which is executed when pilots are detected to be interference-free. Algorithm 1 shows the proposed approach if the estimated T_{rep} indicates a single radar pulse within the data block⁹. The empirical log likelihood function models the hypothesis of noise-only impairment ($P_r = 0$), and is calculated for each non-pilot OFDM symbol. Intuitively, interference-free symbols statistically have a smaller nearest neighbor distance when compared to impaired symbols. In a coherence block, pilot-aided SINR estimates are constant for all REs. As a result, the proposed approach has a high probability of accurately detecting the impaired OFDM symbol.

D. SINR Estimation Using Data Block Reconstruction

If the transmitted symbols are known, then the post-equalizer SINR can be estimated at the receiver perfectly. If $x[n, k] \in \mathcal{X}$ is the transmitted symbol on RE $(n, k) \in \mathcal{D}$, and $y[n, k]$ is the

⁸In sub-6 GHz systems, the typical cyclic prefix duration is 5 – 10 μs . A radar pulse time-aligned with *two consecutive OFDM symbols* will lie within the cyclic prefix (CP) of the second symbol. Due to CP removal in OFDM, radar interference will not impact the second OFDM symbol in such scenarios.

⁹If T_{rep} estimates indicate that m radar pulses will impair the data block, then Algorithm 1 outputs indices corresponding to the m least values.

corresponding post-processed received symbol. The post-processing SINR of RE (n, k) can be directly estimated using

$$\gamma[n, k] = \frac{|x[n, k]|^2}{|x[n, k] - y[n, k]|^2}, \quad (21)$$

and the correspond wideband SINR metrics (average or EESM-based) can be estimated using (6). But $x[n, k]$ can seldom be accurately estimated in the presence of noise interference. However, it can be perfectly reconstructed if the post-decoder bit sequence is known to be accurate.

If \mathbf{b} represents the data bits after turbo-decoding, the receiver can reconstruct the transmitted data symbol on each RE by implementing the transmitter baseband processing chain¹⁰. However, perfect reconstruction is guaranteed only when \mathbf{b} is accurate. In LTE and NR, the integrity of \mathbf{b} is ensured using a cyclic redundancy check (CRC) at the end of each data block, where $\text{CRC} = 0$ (1) indicates decoding success (failure). Since an n -bit CRC has a false positive rate of 2^{-n} , (where $n = 24$ in LTE and NR [21]), we use the CRC as an indicator to accurately reconstruct $x[n, k]$ in our proposed framework.

Remark 2. *If $x_{\text{nn}}[n, k]$ is the nearest neighbor of $y[n, k]$, then $|x[n, k] - y[n, k]|^2 \geq |x_{\text{nn}}[n, k] - y[n, k]|^2$. For constant envelope modulation schemes, post-equalizer SINR estimated using the nearest neighbor decision rule forms an upper bound to the actual SINR. In other QAM schemes, nearest neighbor association often overestimates the SINR.*

E. Numerical Results

In this subsection, we show the performance results of the proposed SINR estimation framework. We consider the example of the LTE-A Pro downlink sharing spectrum with a linear frequency modulated pulsed radar with the transmitted waveform shown in (1), and the other system parameters shown in Table I. In addition, the assumptions used to analytically characterize the heuristic performance in section III are relaxed in the numerical results presented below.

Fig. 5a shows the downlink received power in every subframe. The corresponding windowed FFT computed using a window length of 500 subframes is shown in Fig. 5b. We observe that the amplitude spectrum can accurately estimate $f_{\text{rep}} = \frac{1}{T_{\text{rep}}}$ for a wide range of SIR values.

¹⁰Since 3GPP standardization documents are publicly available [?], it is possible for the receiver to implement the transmitter processing chain if the appropriate control information is decoded correctly.

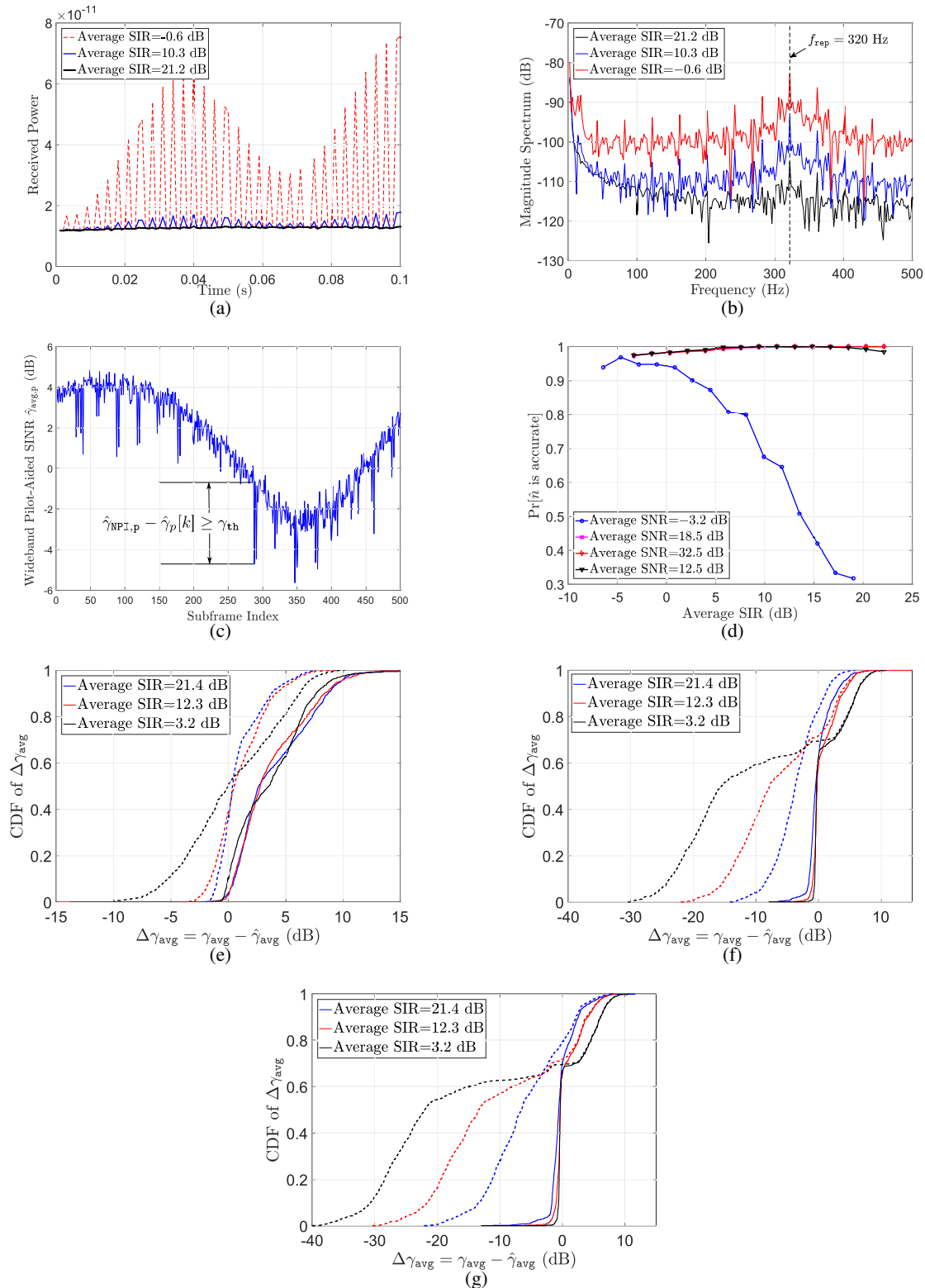


Fig. 5. Performance of various stages of the hybrid post-equalizer SINR estimation framework: (a) received power per subframe in the LTE downlink with average SNR = 19.5 dB, (b) corresponding amplitude spectrum of the received power per subframe for a window length of 500 points, (c) illustration of the threshold-based pilot contamination detection with $\gamma_{\text{th}} = 1$ dB when average SNR = -0.2 dB, (d) probability of accurate *contaminated symbol* detection, and comparison of the average SINR metric mismatch ($\Delta\gamma_{\text{avg}}$ (dB) = γ_{avg} (dB) - $\hat{\gamma}_{\text{avg}}$ (dB)) for interference-impaired subframes using the proposed framework (in solid lines) and the pilot-aided method (in dashed lines) using equation (5), when (e) average SNR = -0.2 dB, (f) average SNR = 13.8 dB, and (g) average SNR = 19.5 dB.

Fig. 5c illustrates the threshold-based pilot contamination detection method described in section IV-B. Using f_{rep} and memory of received power per subframe in the recent past, the pilot-aided wideband SINR ($\hat{\gamma}_{\text{NP I},p}$) is calculated for *interference-free subframes*¹¹, and compared to pilot-aided SINR of the current subframe. As mentioned earlier, a threshold of $\gamma_{\text{th}} = 1$ dB is chosen, since variations greater ± 2 dB will result in use of a different MCS [20].

Fig. 5d shows the performance of Algorithm 1, for different values of SINR. At low SNR, we observe that the accuracy of the proposed method improves with increasing INR when the interference power rises above the noise floor. For medium to high SNRs, the probability of accurate detection is greater than 95%, indicating reliable detection performance for a wide range of SIR and INR values.

Fig. 5e-5g compares SINR estimation performance of the proposed framework ($\hat{\gamma}_{\text{avg,hyb}}$) with the pilot-aided method ($\hat{\gamma}_{\text{avg,p}}$) for *interference-impaired subframes*. The distribution of the average SINR mismatch $\Delta\gamma_{\text{avg}} = (\gamma_{\text{avg}} - \hat{\gamma}_{\text{avg}})$, for a wide range of SNR and INR conditions are plotted, where negative $\Delta\gamma_{\text{avg}}$ indicate overestimated SINR values. We observe that pilot-aided methods have a high density of negative $\Delta\gamma_{\text{avg}}$, that results in degradation of link adaptation performance. In contrast, the proposed framework improves the SINR estimation performance for a large range of SNR and INR values. In the low SNR-high SIR regime, we observe that the proposed framework underestimates the SINR with a probability higher than 95%. This trend can be attributed to the robustness of the heuristic in QPSK, which is typically used in low SINR conditions. In other SNR and SIR regimes, we observe that the semi-blind wideband SINR estimate (a) lies within ± 5 dB of the true value for more than 80% of the subframes, and (b) is skewed towards conservative SINR ($\Delta\gamma_{\text{avg}}$) estimates. As we will demonstrate in the next section, *robust SINR estimates* obtained using the proposed framework significantly improves link-level performance in hostile spectrum sharing environments. However, these improvements are dependent on the availability of accurate SINR estimates for both interference-impaired and interference-free subframes. An explicit scheme to ensure the availability of accurate CSI is presented in the next section.

¹¹If T_{rep} is smaller than the subframe duration, then the received power of *each OFDM symbol* needs to be used to estimate f_{rep} , and detect pilot contamination.

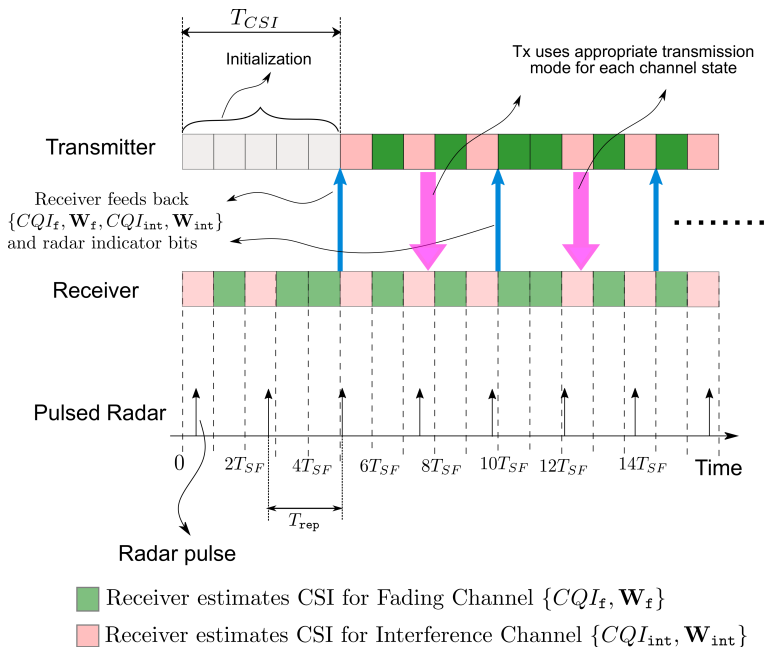


Fig. 6. Illustration of the dual CSI feedback scheme for $T_{CSI} = 5T_{SF}$, where T_{SF} denotes the duration of each data block. The receiver periodically feeds back the CSI for both channel states ($CQI_f, \mathbf{W}_f, CQI_{int}, \mathbf{W}_{int}$), and the radar indicator bits.

V. DUAL CSI FEEDBACK

As discussed in section II-C, current cellular standards support limited CSI feedback of a single set $CSI = \{CQI, \mathbf{W}\}$. While this mechanism is efficient in conventional cellular deployments, the presence of pulsed radar interference in a spectrum sharing scenario results in two channel states:

- 1) the fading channel, in interference-free data blocks, and
- 2) the interference-impaired channel, when the pulsed radar is present.

Clearly, a single set of quantized CSI cannot accurately approximate a bimodal channel distribution. In order to handle the additional state in radar-cellular spectrum sharing, we propose ‘*dual CSI feedback*’, where each user periodically feeds back quantized CSI for both channel states.

A. Feedback Requirements

In the CSI reporting interval, each user feeds back the set $CSI_{dual} = \{CQI_f, \mathbf{W}_f, CQI_{int}, \mathbf{W}_{int}\}$, where the subscript f (int) refers to the CSI of the fading (interference-impaired) channel states respectively.

In addition, the transmitter must know the presence of radar interference in advance, to use the optimal transmission mode for future data blocks. This is enabled by *radar indicator* feedback,

which indicates the presence or absence of pulsed radar in each data block, for the *next* T_{CSI} data blocks. The receiver can predict the presence of radar interference in a future data block by estimating the T_{rep} and monitoring the indices of corrupted OFDM symbols, as discussed in sections IV-A and IV-C. However, it is worthwhile to note that *radar indicator feedback from a single designated user* is enough for the transmitter to know the indices of future corrupted data blocks. Fig. 6 shows a schematic of the dual CSI feedback scheme, where the *initialization procedure* is used to obtain estimates of T_{rep} and CSI_{dual} for the first time.

Assuming a data block duration of $T_{SF} = 1$ ms, if the CSI reporting interval is T_{CSI} , then radar indicator feedback consumes b_{rad} bits of feedback per CSI reporting interval, where $\lceil \log_2(T_{CSI}) \rceil \leq b_{rad} \leq T_{CSI}$ bits. If the number of active users in the cell is N_{act} , the total additional feedback overhead is $b_{int} = (N_{act}N_{int} + b_{rad})$ bits, where N_{int} is the number of additional bits necessary to convey CSI for the interference-impaired fading channel. If $\mathbf{W} \in \mathcal{W}$ and $CQI \in \mathcal{C}$, then $N_{int} \geq \lceil \log_2 |\mathcal{C}| + \log_2 |\mathcal{W}| \rceil$ bits. The corresponding rate overhead is $R_{int} = \frac{N_{act}b_{int}}{T_{CSI}}$ bps.

B. Link-Level Performance Improvements

In this subsection, we compare the performance of the *hybrid SINR estimation-dual CSI feedback* framework with the *pilot-aided SINR estimation-single CSI feedback* scheme (henceforth referred to as the ‘conventional’ scheme). We developed a 3GPP-compliant link-level simulator to analyze radar-LTE coexistence scenarios, using the MATLAB LTE/NR toolboxesTM, using the system parameters shown in Table I. For the conventional scheme, we consider (a) minimum CSI feedback, (b) median CSI feedback, and (c) and maximum CSI feedback schemes that were described in section II-C.

Fig. 7 compares the link-level performance of the proposed framework with the conventional scheme. Fig. 7a shows the throughput as a function of the average INR when the average SNR = 19.5 dB. We observe that the proposed framework achieves a 30% – 100% rate enhancement when compared to median and maximum CSI feedback, and a 47% – 225% rate enhancement compared to minimum CSI feedback. In addition, we also observe that our framework achieves 74% – 96% of the maximum achievable rate over a wide range of INR values, demonstrating a high utilization of the channel capacity.

It is important to observe that the rate improvement due to the proposed framework balances the BLER constraints as shown in Fig. 7b, where $BLER \leq 0.1$ for $INR \leq 12$ dB. Interestingly,

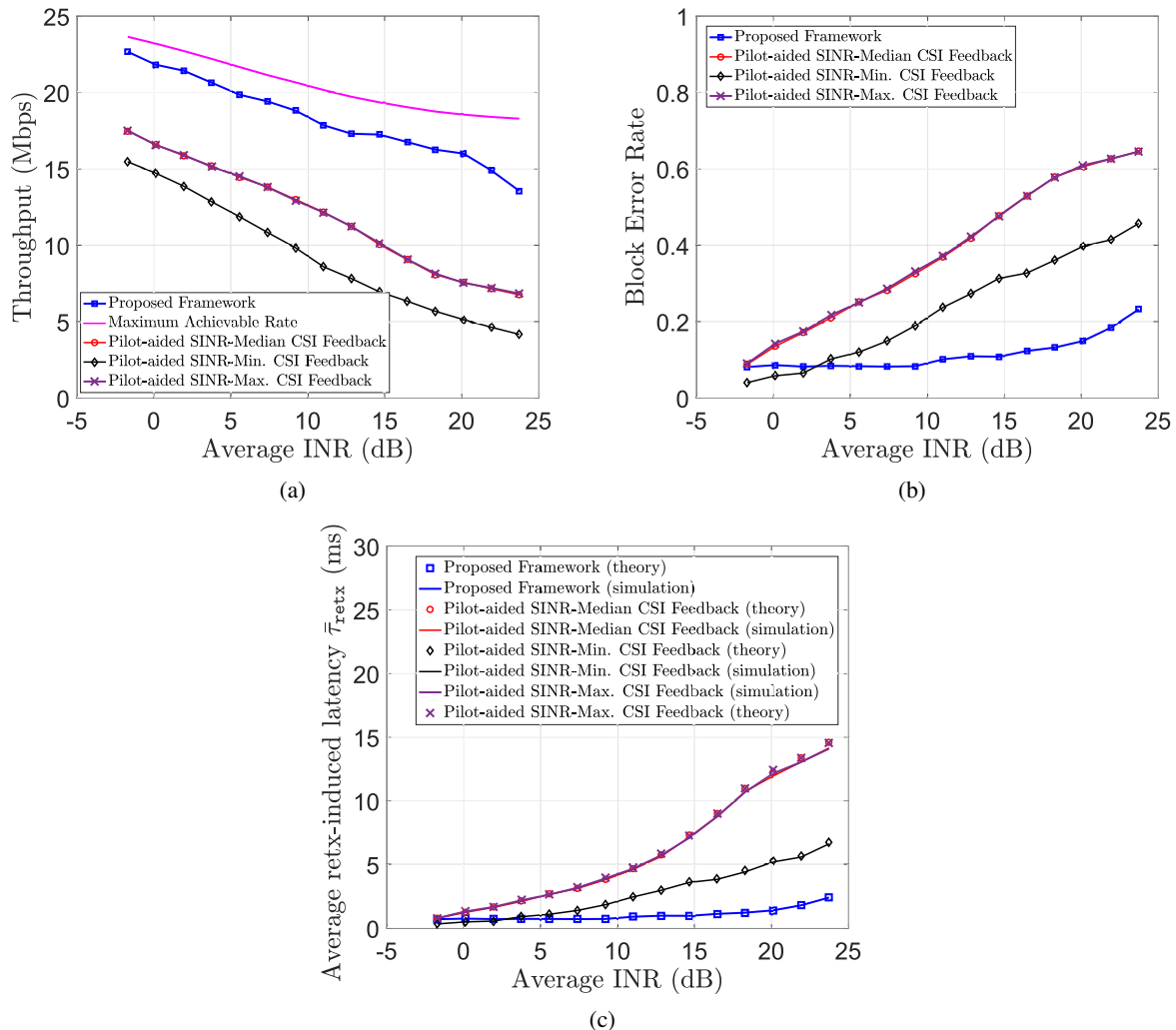


Fig. 7. Enhancement of (a) Throughput, (b) Block Error Rate, and (c) Retransmission-induced latency performance, using the proposed hybrid SINR estimation and Dual CSI feedback framework. The average SNR is 19.5 dB.

the BLER performance at high INR improves significantly when compared to minimum CSI feedback, the most conservative conventional scheme. As expected, median and maximum CSI feedback always result in a higher BLER compared to minimum CSI feedback. This is because it requires a higher number of interference-impaired pilots per estimation window to mimic the performance of minimum CSI feedback.

High BLER due to decoding failures result in degradation of the *HARQ-induced latency*, which is defined as the latency due to hybrid ARQ (HARQ) retransmissions in LTE and NR. The average HARQ-induced latency ($\bar{\tau}_{\text{retx}}$) is approximately given by [23]

$$\bar{\tau}_{\text{retx}} = \frac{\text{BLER} \times \bar{\tau}_{\text{wait}}}{1 - \text{BLER}}. \quad (22)$$

$\bar{\tau}_{\text{wait}}$ is the average wait time between consecutive retransmissions. We assume $\bar{\tau}_{\text{wait}} = 8$ ms, which is the typical value in LTE and NR [19], [21]. Fig. 7c shows that the proposed framework improves retransmission induced latency by a factor of 3 when compared to minimum CSI feedback, and by an order of magnitude when compared to median CSI feedback. In addition, we observe that theoretical and simulation values are in good agreement.

In LTE and NR, CSI feedback for single-user transmission modes has a overhead of about $b_{\text{fb}} = 10$ bits per CSI estimation interval T_{CSI} , where $T_{\text{CSI}} \geq 2$ ms [21], [19]. Therefore, in a cell with $N_{\text{act}} = 100$ active users, the additional rate overhead due to dual CSI feedback will satisfy $r_{\text{int}} \leq \frac{100 \times (10)}{2 \times 10^{-3}} + \frac{1}{1 \times 10^{-3}} = 510$ kbps.

In summary, the proposed framework simultaneously improves throughput, BLER, and latency performance when compared to conventional schemes in the presence of pulsed radar interference. For most operational regimes, the downlink throughput improvement is significantly high to justify the use of dual CSI feedback. For MU-MIMO transmission modes in NR that typically need 100 bits/user/CSI estimation interval [21], further investigation is needed to evaluate the performance achieved using our framework. In general, dual CSI feedback is beneficial if the *cell-wide throughput gain* is greater than the additional uplink rate overhead.

VI. CONCLUSION

In this paper, we developed a comprehensive semi-blind SINR estimation framework using pilot-aided and heuristic-aided estimates to compute the wideband post-equalizer SINR in radar-cellular coexistence scenarios. We characterized the distribution of a low complexity max-min heuristic under a tractable signal model, and demonstrated its accuracy and robustness for interference-impaired QAM data symbols. To handle channel bimodality due to periodic transitions between the *fading* and the *interference-impaired* channel states, we proposed a *dual CSI feedback* mechanism where the receiver reports quantized CSI for both channel states. Unifying these two schemes and using radar-LTE-A Pro coexistence as an example, we demonstrated significant improvements in key link-level performance metrics such as throughput, BLER and retransmission-induced latency *simultaneously*.

In vehicular communication systems such as C-V2X, link adaptation decisions need to be taken at a faster timescale due to the highly dynamic wireless channel. Co-channel or adjacent channel pulsed radar interference inhibits accurate CSI acquisition, which adversely impacts the rate and latency performance of a vehicular link. The semi-blind SINR estimation and dual CSI

feedback framework proposed in this paper addresses the issue of accurate CSI acquisition in the presence of such wideband intermittent interference signals. Further, the low computational complexity and low overhead of the proposed framework promises a high potential for being effective in dynamic channel conditions, and hence is attractive for implementation in vehicular communication systems sharing spectrum with a high-powered radar.

Investigation of the optimal SU- and MU-MIMO precoder estimation in non-pilot interference is a useful extension to this work, which is especially important in multi-antenna transmission modes of LTE-A Pro and 5G NR. In addition, novel scheduling and resource management schemes based on this framework can also be developed for different applications such as vehicular-to-everything (V2X) and Internet of Things (IoT) services coexisting with radar. Such scenario-specific frameworks will be of practical importance to enable efficient link adaptation mechanisms in radar-5G/6G coexistence since rate and latency performance often need to be jointly optimized in these scenarios.

APPENDIX

PROOF OF LEMMA 1

The conditional CDF of $\{D|X, \Phi\}$ can be written as

$$F_D(d|x, \phi) = \int_{\mathcal{A}_{n_R}} \int_{\mathcal{A}_{n_I}} \mathbb{P}[D \leq d|x, \phi, n] f_N(n) dn,$$

where $f_N(n) = f_{N_R}(n_R) f_{N_I}(n_I)$. By equation (12) we can observe that D is a Rician random variable, since it is the amplitude of a complex Gaussian where the real/imaginary parts have a different mean. Thus, the integral can be transformed into polar coordinates (z, θ) to get an integral of the form

$$F_D(d|x, \phi) = \int_0^d \int_{\mathcal{A}_\theta(z)} f_{Z,\Theta}(z, \theta|x, \phi) d\theta dz, d \geq 0, \quad (23)$$

where $f_{Z,\Theta}(z, \theta|x, \phi)$ is the conditional density function of $\{Z, \Theta\}$. Depending on the value of D , there are 3 distinct regions of integration for QAM constellations: (a) $0 \leq d \leq \frac{d_c}{2} \forall x \in \mathcal{X}$, (b) $\frac{d_c}{2} \leq d \leq \frac{d_c}{\sqrt{2}} \forall x \in \mathcal{X}$, and (c) $\frac{d_c}{\sqrt{2}} \leq d \leq +\infty$ for $x \in \mathcal{X}_{\text{bnd}}$. Fig. 8 shows these regions for 16-QAM. We denote the distance of each point $x_i \in \mathcal{X}$ along the x- and y-axes to the edges of its decision region is given by $d_{x_i}^{L,R}$, $d_{x_i}^{U,R}$ and $d_{x_i}^{L,I}$, $d_{x_i}^{U,I}$ respectively. Table II shows these boundaries for points in the first quadrant of a 16-QAM constellation. Below, we derive the conditional distribution of $\{D|X, \Phi\}$ for each region, by leveraging the properties of Rician r.v's.

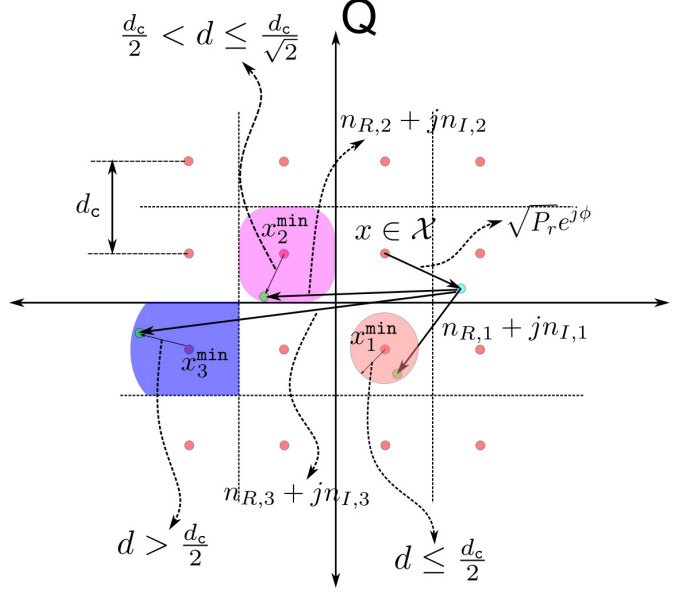


Fig. 8. Illustration of the different range of values for d , and the corresponding region of integration to derive $F_D(d)$. Cases 1 and 2 are possible for all $x \in \mathcal{X}$, but case 3 is possible only for $x \in \mathcal{X}_{\text{bdry}}$.

A. Case 1: $0 \leq d \leq \frac{d_c}{2} \forall x^{(j)} \in \mathcal{X}$

In this case, the region of integration is *circular* with radius d as shown in Fig. 8 (red shaded region). Defining $m_{R,j} \triangleq [x_R - x_R^{(j)} + \sqrt{P_r} \cos(\phi) + n_R]$, $m_{I,j} \triangleq [x_I - x_I^{(j)} + \sqrt{P_r} \sin(\phi) + n_I]$, and $\theta \triangleq \tan^{-1} \left(\frac{m_{I,j}}{m_{R,j}} \right)$ in equation (12), and conditioning on $x, x^{(j)} \in \mathcal{X}$ and $\phi \in [0, 2\pi]$, we observe that when the nearest neighbor is $x^{(j)} \in \mathcal{X}$, $\{D_{\min}|X, \phi\} \sim \text{Rician}(\nu_j, \sigma^2)$ with parameters $\nu_j^2 = m_{R,j}^2 + m_{I,j}^2$ and $\sigma^2 = \frac{\sigma_n^2}{2}$. Therefore, we have

$$\begin{aligned}
 f_Z(z|x, \phi) &= \sum_{x^{(j)} \in \mathcal{X}} \frac{2z}{\sigma_n^2} e^{-\frac{z^2 + \nu_j^2}{\sigma_n^2}} I_0\left(\frac{2\nu_j z}{\sigma_n^2}\right), z \geq 0, \text{ and} \\
 F_D(d|x, \phi) &= \sum_{x^{(j)} \in \mathcal{X}} \int_0^d \frac{2z}{\sigma_n^2} e^{-\frac{z^2 + \nu_j^2}{\sigma_n^2}} I_0\left(\frac{2\nu_j z}{\sigma_n^2}\right) dz, \\
 &\stackrel{(a)}{=} \sum_{x^{(j)} \in \mathcal{X}} \left[1 - Q_1\left(\frac{\sqrt{2}\nu_j}{\sigma_n}, \frac{\sqrt{2}d}{\sigma_n}\right) \right], \tag{24}
 \end{aligned}$$

where $I_0(\cdot)$ is the Bessel function of the first kind with order zero, and (a) is obtained by simplifying the CDF of a Rician random variable in the form of a Marcum Q-function with parameters (M, a, b) [35].

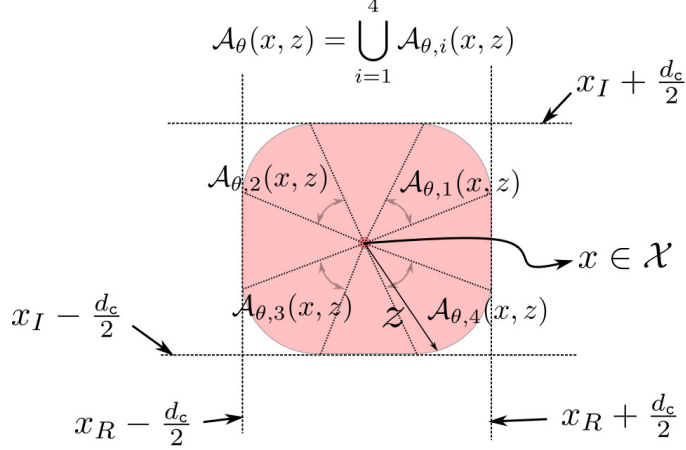


Fig. 9. Illustration of the limits of θ in equation (26) when $x \in \mathcal{X}_{\text{int}}$.

B. Case 2: $\frac{d_c}{2} \leq d \leq \frac{d_c}{\sqrt{2}} \forall x^{(j)} \in \mathcal{X}$

In this case, the integration region for each point x_j is a ‘truncated’ circle, as shown in Fig. 8 (pink colored region). The minimum distance D is a Rician random variable with a *radially asymmetric integration region*. Therefore, the conditional density in polar coordinates is given by

$$f_{Z,\Theta}(z, \theta | x, \phi) = \sum_{x^{(j)} \in \mathcal{X}} \frac{z}{\pi \sigma_n^2} e^{-\frac{z^2 + \nu_j^2 + 2zm_j}{\sigma_n^2}}, \quad (25)$$

for $z \geq 0, 0 \leq \theta \leq 2\pi$. The region of integration of Θ for $x \in \mathcal{X}$ is a function of z , given by

$$\mathcal{A}_\theta(x, z) = \left\{ \theta \mid d_x^{L,R} \leq z \cos \theta \leq d_x^{U,R}, d_x^{L,I} \leq z \sin \theta \leq d_x^{U,I} \right\}.$$

For $x \in \mathcal{X}_{\text{int}}$, the above can be simplified as

$$\begin{aligned} \mathcal{A}_\theta(x, z) &= \bigcup_{i=1}^4 \mathcal{A}_{\theta,i}(x, z), \text{ where} \\ \mathcal{A}_{\theta,i}(x, z) &= \left\{ \theta \mid (i-1)\frac{\pi}{2} + \cos^{-1}\left(\frac{d_c}{2z}\right) \leq \theta \leq (i-1)\frac{\pi}{2} + \sin^{-1}\left(\frac{d_c}{2z}\right) \right\}. \end{aligned} \quad (26)$$

Fig. 9 shows an example of the integration region for $x^{(j)} \in \mathcal{X}_{\text{int}}$. Using (25)-(26) and marginalizing Θ and X , we obtain the desired result.

C. Cases 3 and 4: $d \geq \frac{d_c}{\sqrt{2}}$ for all $x^{(j)} \in \mathcal{X}$

Derivation of the conditional CDF is similar to that in Case 2. The additional constraint here is that $F_{D|X,\Phi}(d|x, \phi)$ is non-zero iff $x^{(j)} \in \mathcal{X}_{\text{bnd}}$. This is because for interior points, $0 \leq D_{\text{min}} \leq \frac{d_c}{\sqrt{2}}$ is always true for QAM modulation schemes, as illustrated in Fig. 8.

REFERENCES

- [1] FCC, “Amendment of the Commission’s Rules with Regard to Commercial Operations in the 3550-3650 MHz Band,” *Federal Communications Commission, Report and Order and Second Further Notice of Proposed Rulemaking*, April 2015.
- [2] FCC, “Revision of Part 15 of the Commission’s Rules to Permit Unlicensed National Information Infrastructure (U-NII) Devices in the 5 GHz Band,” *Federal Communications Commission, First Report and Order*, April 2014.
- [3] Michael Kratsios, “Emerging Technologies and their Expected Impact on Non-Federal Spectrum Demand,” *Executive Office of the President of the United States*, May 2019.
- [4] W. L. Ross, “Annual Report on the Status of Spectrum Repurposing,” August 2019. [Online]. Available: https://www.ntia.doc.gov/files/ntia/publications/spectrum_repurposing_report_august_2019.pdf
- [5] H. Kwon, J. Jeon, A. Bhorkar, Q. Ye, H. Harada, Y. Jiang, L. Liu, S. Nagata, B. L. Ng, T. Novlan, J. Oh, and W. Yi, “Licensed-Assisted Access to Unlicensed Spectrum in LTE Release 13,” *IEEE Communications Magazine*, vol. 55, no. 2, pp. 201–207, February 2017.
- [6] 3GPP, “LTE; Evolved Universal Terrestrial Radio Access (E-UTRA); Physical layer procedures (release 14),” *ETSI TS 136 213 v14.3.0*, June 2017.
- [7] G. Naik, B. Choudhury, and J. Park, “IEEE 802.11bd 5G NR V2X: Evolution of Radio Access Technologies for V2X Communications,” *IEEE Access*, vol. 7, pp. 70 169–70 184, 2019.
- [8] A. Khawar, A. Abdel-Hadi, and T. C. Clancy, “Spectrum Sharing between S-band Radar and LTE Cellular System: A Spatial Approach,” in *IEEE International Symposium on Dynamic Spectrum Access Networks (DYSPAN)*, April 2014, pp. 7–14.
- [9] J. A. Mahal, A. Khawar, A. Abdelhadi, and T. C. Clancy, “Spectral Coexistence of MIMO Radar and MIMO Cellular System,” *IEEE Transactions on Aerospace and Electronic Systems*, vol. 53, no. 2, pp. 655–668, April 2017.
- [10] F. Liu, C. Masouros, A. Li, and T. Ratnarajah, “Robust MIMO Beamforming for Cellular and Radar Coexistence,” *IEEE Wireless Communications Letters*, vol. 6, no. 3, pp. 374–377, June 2017.
- [11] B. Li, A. P. Petropulu, and W. Trappe, “Optimum Co-Design for Spectrum Sharing between Matrix Completion Based MIMO Radars and a MIMO Communication System,” *IEEE Transactions on Signal Processing*, vol. 64, no. 17, pp. 4562–4575, Sep. 2016.
- [12] B. Tang and J. Li, “Spectrally Constrained MIMO Radar Waveform Design Based on Mutual Information,” *IEEE Transactions on Signal Processing*, vol. 67, no. 3, pp. 821–834, Feb 2019.
- [13] S. Kim, J. Choi, and C. Dietrich, “PSUN: An OFDM-Pulsed Radar Coexistence Technique with Application to 3.5 GHz LTE,” *Mobile Information Systems*, vol. 2016, 2016.
- [14] M. Carrick, J. H. Reed, and C. M. Spooner, “Mitigating Linear-Frequency-Modulated Pulsed Radar Interference to OFDM,” *IEEE Transactions on Aerospace and Electronic Systems*, vol. 55, no. 3, pp. 1146–1159, June 2019.
- [15] R. Saruthirathanaworakun, J. M. Peha, and L. M. Correia, “Opportunistic Sharing Between Rotating Radar and Cellular,” *IEEE Journal on Selected Areas in Communications*, vol. 30, no. 10, pp. 1900–1910, November 2012.
- [16] Z. Khan, J. J. Lehtomaki, R. Vuoltoniemi, E. Hossain, and L. A. DaSilva, “On Opportunistic Spectrum Access in Radar Bands: Lessons Learned from Measurement of Weather Radar Signals,” *IEEE Wireless Communications*, vol. 23, no. 3, pp. 40–48, June 2016.
- [17] M. Ghorbanzadeh, E. Visotsky, P. Moorut, and C. Clancy, “Radar Interference into LTE Base Stations in the 3.5 GHz Band,” *Physical Communication*, vol. 20, pp. 33–47, 2016.
- [18] J. H. Reed, A. W. Clegg, A. V. Padaki, T. Yang, R. Nealy, C. Dietrich, C. R. Anderson, and D. M. Mearns, “On the

- Co-Existence of TD-LTE and Radar Over 3.5 GHz Band: An Experimental Study,” *IEEE Wireless Communications Letters*, vol. 5, no. 4, pp. 368–371, Aug 2016.
- [19] S. Sesia, M. Baker, and I. Toufik, *LTE-The UMTS Long Term Evolution: From Theory to Practice*. John Wiley & Sons, 2011.
- [20] M. Rupp, S. Black, and M. Taranetz, *The Vienna LTE-Advanced Simulator*. Springer, 2016, vol. 31.
- [21] E. Dahlman, S. Parkvall, and J. Skold, *5G NR: The Next Generation Wireless Access Technology*. Academic Press, 2018.
- [22] E. Charles and B. Marvin, “Radar Signals: An Introduction to Theory and Application,” *Artech House*, 1993.
- [23] R. M. Rao, V. Marojevic, and J. H. Reed, “Analysis of Non-Pilot Interference on Link Adaptation and Latency in Cellular Networks,” in *IEEE 89th Vehicular Technology Conference (VTC2019-Spring)*, April 2019, pp. 1–5.
- [24] H. Safavi-Naeini, C. Ghosh, E. Visotsky, R. Ratasuk, and S. Roy, “Impact and Mitigation of Narrow-band Radar Interference in Downlink LTE,” in *2015 IEEE International Conference on Communications (ICC)*, June 2015, pp. 2644–2649.
- [25] R. M. Rao, V. Marojevic, and J. H. Reed, “Probability of Pilot Interference in Pulsed Radar-Cellular Coexistence: Fundamental Insights on Demodulation and Limited CSI Feedback,” *IEEE Communications Letters*, to appear, 2020. [Online]. Available: <https://arxiv.org/abs/2005.00122>
- [26] S. Baumgartner and G. Hirtz, “A Blind ML-SNR Estimation Method for OFDM Systems in Dispersive Fading Channels,” in *IEEE 4th International Conference on Consumer Electronics Berlin (ICCE-Berlin)*, Sept 2014, pp. 475–479.
- [27] F. X. Socheleau, A. Aissa-El-Bey, and S. Houcke, “Non Data-aided SNR Estimation of OFDM Signals,” *IEEE Communications Letters*, vol. 12, no. 11, pp. 813–815, November 2008.
- [28] Y. Chen and N. C. Beaulieu, “NDA Estimation of SINR for QAM Signals,” *IEEE Communications Letters*, vol. 9, no. 8, pp. 688–690, Aug 2005.
- [29] S. Hong, Y. Li, Y. C. He, G. Wang, and M. Jin, “A Cyclic Correlation-Based Blind SINR Estimation for OFDM Systems,” *IEEE Communications Letters*, vol. 16, no. 11, pp. 1832–1835, November 2012.
- [30] S. K. Pulliyakode, S. Kalyani, and K. Narendran, “Rate Prediction and Selection in LTE Systems Using Modified Source Encoding Techniques,” *IEEE Transactions on Wireless Communications*, vol. 15, no. 1, pp. 416–429, Jan 2016.
- [31] A. M. Mansour, A. E. R. Nada, and A. H. Mehana, “Effect of Noise Variance Estimation on Channel Quality Indicator in LTE Systems,” in *IEEE Global Conference on Signal and Information Processing (GlobalSIP)*, Dec 2015, pp. 156–160.
- [32] Ping Li, D. Paul, R. Narasimhan, and J. Cioffi, “On the Distribution of SINR for the MMSE MIMO Receiver and Performance Analysis,” *IEEE Transactions on Information Theory*, vol. 52, no. 1, pp. 271–286, Jan 2006.
- [33] S. N. Donthi and N. B. Mehta, “An Accurate Model for EESM and its Application to Analysis of CQI Feedback Schemes and Scheduling in LTE,” *IEEE Transactions on Wireless Communications*, vol. 10, no. 10, pp. 3436–3448, October 2011.
- [34] R. C. Daniels, C. M. Caramanis, and R. W. Heath, “Adaptation in Convolutionally Coded MIMO-OFDM Wireless Systems Through Supervised Learning and SNR Ordering,” *IEEE Transactions on Vehicular Technology*, vol. 59, no. 1, pp. 114–126, Jan 2010.
- [35] M. Abramowitz and I. A. Stegun, *Handbook of Mathematical Functions: with Formulas, Graphs, and Mathematical Tables*. Courier Corporation, 2012.